Crustal Seismogenic Thickness and Thermal Structure of NW South America

Ángela María Gómez-García[1,2,+], Álvaro González[1,3], Mauro Cacace[1], Magdalena Scheck-Wenderoth[1], Gaspar Monsalve[4]

[1] GFZ German Research Centre for Geosciences. Telegrafenberg, 14473, Potsdam, Germany.

[2] Corporation Center of Excellence in Marine Sciences (CEMarin). Bogotá, Colombia.

[3] Centre de Recerca Matemàtica (CRM). Campus UAB, Edifici C. 08193, Bellaterra (Barcelona), Spain.

[4] Universidad Nacional de Colombia, Facultad de Minas, Medellín, Colombia.

Corresponding author: Ángela María Gómez-García (angela@gfz-potsdam.de). [+]Now at Geosciences Barcelona (GEO3BCN), CSIC, Lluís Solé i Sabarís s/n. 08028, Barcelona, Spain

Abstract. The crustal seismogenic thickness (CST) has direct implications on the magnitude and occurrence of crustal earthquakes, and therefore, on the seismic hazard of any region. Amongst other factors, the seismogenesis of rocks is affected by in-situ conditions (temperature and state of stress) and by the rocks' heterogeneous composition. Diverse laboratory experiments have explored the frictional behavior of the most common materials forming the crust and uppermost mantle. However, it remains a matter of debate how to "up-scale" to the scale of the crust the conclusions derived from these studies. In this study we propose a workflow to up-scale and validate these experiments to natural geological conditions of crustal and upper mantle rocks. We used NW South America as a case study to explore the three-dimensional spatial variation of the CST and the potential temperatures at which crustal earthquakes occur. The 3D steady-state thermal field was computed with a finite element scheme using the software GOLEM, taking into account the uppermost 75 km of a previously published 3D data-integrated lithospheric configuration and lithology-constrained thermal parameters. We found that the majority of events nucleate at temperatures of less than 350°C, in general agreement with frictional experiments of crustal and mantle materials. A few outliers in the hypocentral temperatures showcase nucleation conditions consistent with the seismogenic window of olivine-rich rocks, and can be linked to uncertainties in the Moho depths and/or in the earthquake hypocenters, or to the presence of ultramafic rocks within the allochthonous crustal terranes accreted to this complex margin. Our results suggest that the two largest earthquakes recorded in the region (*Ms*=6.8 and *Ms*=7.3, Murindó sequence, in 1992) nucleated at the calculated lower boundary of the seismogenic crust, highlighting the importance of considering this transition when characterizing the seismogenic source in hazard assessment studies. The approach presented in this study can be applied to other tectonic settings worldwide, and it could be further refined as new, high-quality heat flow and temperature observations became eventually available for testing and validating the thermal models.
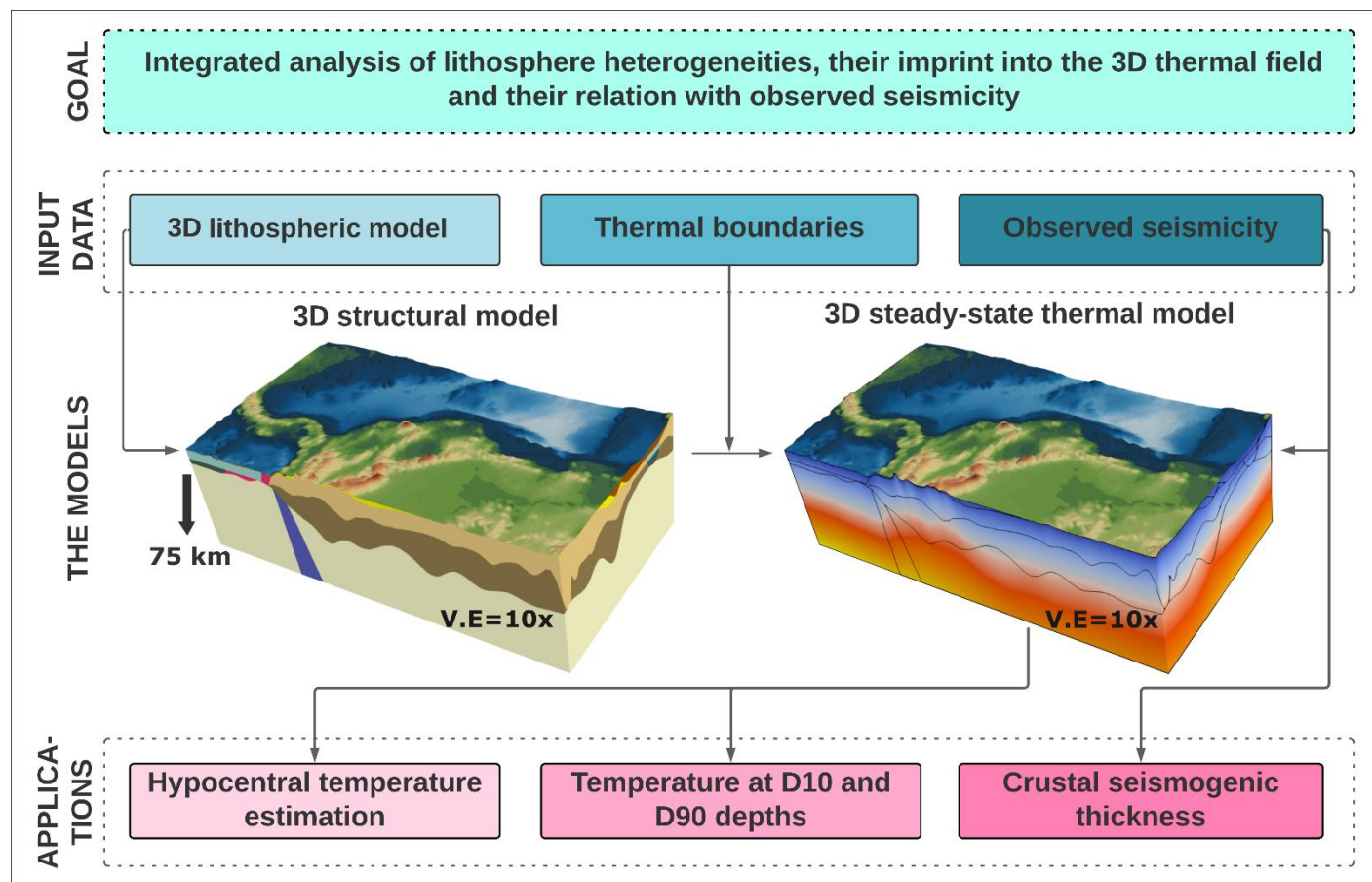
1 Introduction

The crustal seismogenic thickness (CST) encloses the portion of the crust where the majority of earthquakes occur. Its upper boundary, hereafter referred to as the upper stability transition (UST), demarks the onset depth of seismicity. Its lower boundary, referred to as the lower stability transition (LST), defines the cutoff depth of seismicity (Marone & Saffer, 2015; Marone & Scholz, 1988; Scholz, 2019; Wu et al., 2017). The LST can also be used as a conservative upper estimate of the brittle-ductile transition (BTD) (e.g.: Zuza & Cao, 2020). The depths of both the UST and the LST are usually determined based on imposed percentiles of the statistical distribution of earthquake hypocentral depths (e.g.: Marone & Scholz, 1988; Sibson, 1982; Wu et al., 2017). The seismogenic crust is then defined as the portion of the crust that contains a prescribed (i.e., statistically significant) percentage of the recorded earthquakes.

The spatial distribution of seismicity is controlled by the mechanical properties of the hosting crustal rocks, and therefore by factors such as composition, grain size and mineral assemblage, as well as by the in-situ temperature, pressure and strain rates conditions (e.g. Chen et al., 2013; Zielke et al., 2020). Laboratory experiments are indicative of a range of limiting temperatures for seismogenesis, i.e.: temperatures at which rocks and mineral assemblies exhibit stick-slip behavior. For example, granitic rocks exhibit seismic behavior at temperatures between 90-350°C, gabbro between 200 and 600°C, and olivine gouge between 600 and 1000°C (Scholz, 2019, and references therein). Apart from subduction zones, it is generally considered that earthquakes nucleate within the crust at < 350±50°C, and at < 700±100°C in the mantle (see review by Chen et al., 2013).

As an attempt to up-scale the results of laboratory experiments, previous studies have aimed at modelling the thermal field of active systems targeting the temperature ranges at which earthquakes can nucleate (e.g.: Gutscher et al., 2016; Oleskevich et al., 1999; Zuza & Cao, 2020). The results from these efforts suggest that in faults located within the continents, the BDT seems to be controlled by variations in the geothermal gradient, being limited by the 300-350°C isotherm, consistent with a quartz-dominated lithology (e.g.: Zuza & Cao, 2020). Nevertheless, most of these approaches usually consider a simplified lithospheric structure, disregarding particular tectonic assemblies that can considerably affect the three-dimensional configuration of the thermal field (e.g. Cacace and Scheck-Wenderoth, 2016). Moreover, the majority of studies have targeted preferentially regions away from active subduction zones (Chen et al., 2013).

In this paper, we systematically map the CST and the temperatures at which crustal earthquakes nucleate in the South Caribbean and NW South America (Fig. 1). The complex tectonic setting poses a challenge to compare the results from laboratory experiments, including the convergence of at least four tectonic plates, the accretion of several allochthonous terranes, and the presence of continental sedimentary basins with thicknesses of up to 8 km (Mora-Bohórquez et al., 2020). Although few events with magnitude $M > 7.0$ have been recorded in northern South America since the deployment of modern seismological networks, there are historical records of earlier great earthquakes, for example, the shock which destroyed the city of Santa Marta, Colombia, in 1834. Similarly, paleoseismological studies in western Venezuela found fault rupture of other events with estimated magnitudes $M > 7.0$ (e.g.: Audemard, 1996; Pousse-Beltran et al., 2018). Overall, there is a substantial seismic hazard in this region (Arcila et al., 2020; Pagani et al., 2018), and large population centers are located close to shallow active faults, which are able to generate devastating earthquakes (Veloza et al., 2012). As a result, there is a high seismic risk (Silva et al., 2018). Therefore, it is expected that a better understanding of the regional seismogenesis will significantly contribute to future seismic hazard and risk assessments.

Here we rely on seismic events with the highest quality hypocentral depths reported in the ISC Bulletin since 1980 (International Seismological Centre, 2022) for mapping the spatially-variable depths to the UST, LST, and the CST. We do not attempt to account for transient changes in the seismogenic zone configuration, but rather focus on quantifying the regional variotions of these transitions averaged over time, considering lithological and structural heterogeneities.

As the extend of the CST is influenced by spatially heterogeneous factors such as lithology and local geothermal gradients (Hirth and Beeler, 2015; Zielke et al., 2020), we computed the 3D steady-state thermal response using a recently published 3D structural and density model of the study area that is consistent with different geological and geophysical observations including gravity (Gómez-García et al., 2020, 2021). A steady-state approach can be regarded as appropriate for this analysis since we preferentially target crustal earthquakes, and because the subducting segments of the Nazca and Caribbean slabs in the study area are flat (Gómez-García et al., 2021; Kellogg et al., 2019; Sun et al., 2022). In order for this approach to be realistic, our thermal model considers only the uppermost 75 km of the lithosphere. Besides the lithospheric-scale structural model, the main input for our thermal calculations are lithology-dependent thermal properties for the different layers of the lithosphere, the average temperature field on the Earth's surface as an upper boundary condition and the temperatures at 75 km depth, used as the lower boundary condition. This lower thermal boundary condition has been derived from the SL2013sv tomographic model of Schaeffer and Lebedev (2013) using a petrophysical parametrization, which actually indirectly takes into account possible non-steady-state effects of thermal transport, expected to be non-negligible at deeper realms due to mantle convection.

From the 3D thermal model, calibrated with the available heat flow and borehole temperature observations, we extracted the temperatures at the UST and LST from the 3D thermal model, as well as at the hypocentral depths of the seismic events. Our approach could be refined as more observations became available for calibrating the thermal model. Its main advantage is to provide a comprehensive view of the system's heterogeneities, their contribution to the thermal field, and the long-term geological timescale given by the mantle thermal contribution and the 3D present-day lithospheric configuration.

2 Study area

The study area (5°-15°N and 63°-82°W, Fig. 1) includes the interaction of the Caribbean and Nazca (Coiba) flat-slabs at depth (Gómez-García et al., 2021; Kellogg et al., 2019; Sun et al., 2022). Due to this interaction, a complex tectonic setting is present at lithospheric-scale, including large uncertainties in depths to the Moho interface (e.g.: Avellaneda-Jiménez et al., 2022; Poveda et al., 2015; Reguzzoni & Sampietro,ta 2015).

Figure 1. depicts the crustal seismic catalogue derived from the ISC Bulletin (International Seismological Centre, 2022, see Sect. 3.2.1), and active fault traces. For the sake of clarity, in the remaining of the study we will focus on three specific sub-regions, marked by blue boxes in Fig. 1. Our choice stems from the fact that these regions have contrasting tectonic

environments, a heterogeneous spatial distribution of crustal seismicity and diverse allochthonous terranes accreted to the NW margin of South America (see Montes et al., 2019).
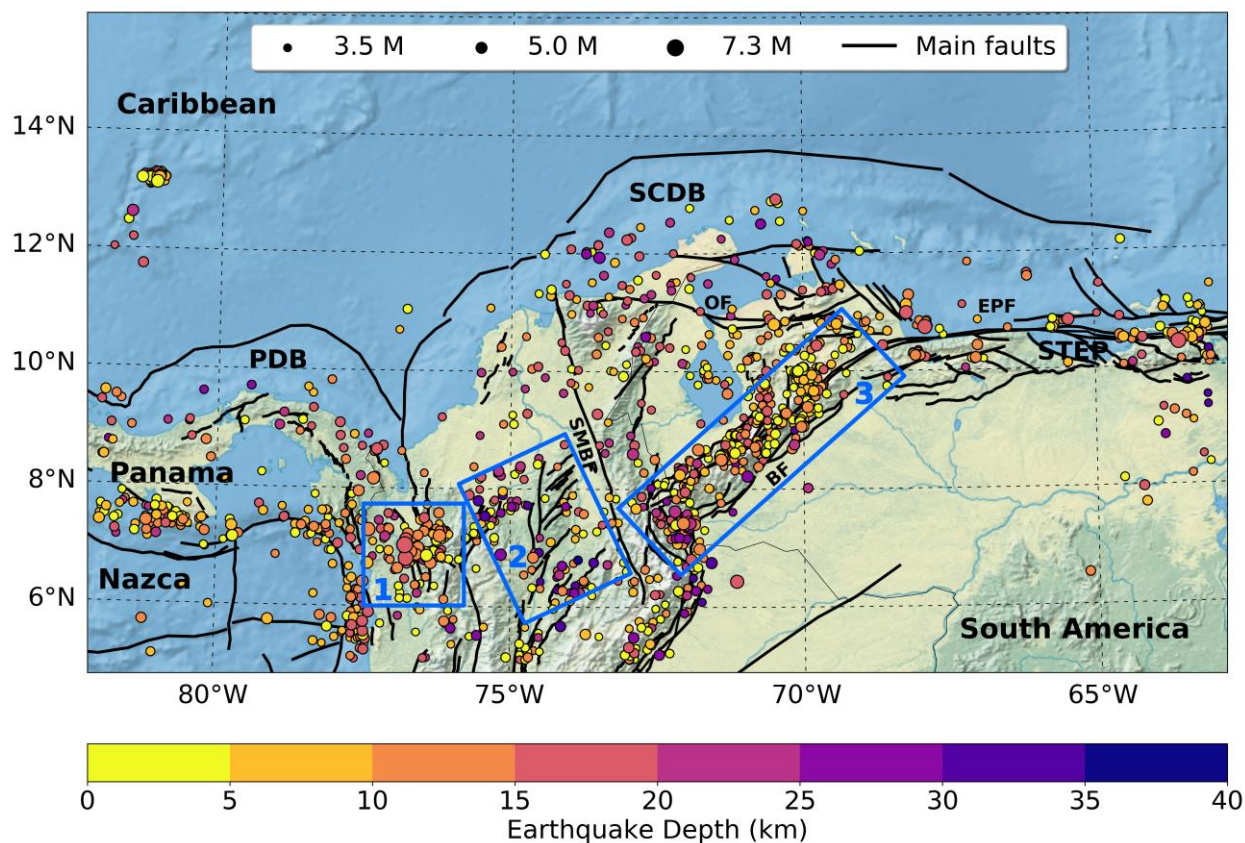
Figure 1. Crustal earthquakes with the best determined hypocentral depths in the region, selected from the ISC Bulletin (International Seismological Centre, 2022) as detailed in Sect. 3.2.1. Blue boxes: Sub-regions discussed in the main text. Black lines: Active fault traces as compiled by Styron et al. (2020) and Veloza et al. (2012). PDB = Panama deformed belt, SCDB = South Caribbean Deformed Belt and STEP = Subduction-Transform-Edge-Propagator fault system. Main fault systems are: BF = Boconó Fault, SMBF = Santa Marta - Bucaramanga Fault, EPF = El Pilar Fault, and OF = Oca-Ancon Fault.

Region 1 corresponds to the area around the Murindó seismic cluster (Dionicio and Sánchez, 2012). In this region, the Uramita fault system (UF, Fig. 3) acts as the suture between the (mainly) oceanic terranes of the western Cordillera, and the Panamá-Chocó block, dominated by plateau and magmatic arc terranes (León et al., 2018; Montes et al., 2019; Mosquera-Machado et al., 2009). Diverse active faults have been described in this area, including the Atrato, Mutatá and Murindó systems (MF, Fig. 3). The latter has been considered responsible for the M_s = 6.8 foreshock and M_s = 7.3 mainshock events, on 17th

and 18th October 1992, respectively (Mosquera-Machado et al., 2009), the largest earthquakes recorded in the study region since the 1980s. The mainshock caused widespread liquefaction, landslides, complete destruction of the center of Murindó town and even building damages in Medellín, a city located more than 130 km away from the epicenter (Mosquera-Machado et al., 2009; Martínez et al., 1994). In terms of recorded seismicity, this region is characterized by a dense occurrence of earthquakes at depths shallower than 25km.

Region 2 includes the Otú, Palestina and El Espíritu Santo fault systems (Paris et al., 2000). The Palestina fault is a NE-SW strike-slip, right-lateral system that cuts the Central Cordillera, and its formation may have been associated to the oblique subduction of the oceanic lithosphere during the Late Cretaceous (Acosta et al., 2007). This system can be interpreted as the northward continuation of a large-scale brittle suture of different terranes (Kennan and Pindell, 2009). In this study, we grouped the Palestina and Otú-Pericos faults in what we will refer to as the Otú-Palestina fault system (OPF, Fig. 3), even though those two structures might be genetically different (Restrepo & Toussaint, 1988). The right-lateral Espíritu Santo fault (ES, Fig. 3) can be considered as a part of the large-scale suture zone defined by the Romeral Fault System (Noriega-Londoño et al., 2020). This region concentrates most of the deepest seismic events of the study area.

Lastly, Region 3 comprises the Venezuelan Andes including the NE-SW Boconó fault system (BF, Fig. 1). This active fault network accommodates most of the Maracaibo block displacement with a right-lateral strike-slip motion, and serves as its boundary with South America (Pousse-Beltran et al., 2018 and references therein). The seismicity is deeper in the SW portion of the fault system and shows a smooth transition where it shallows towards the NE (Fig. 1).

3 Methods

3.1 Steady-state 3D thermal model and input data

The main mechanism of heat transport within the lithosphere is thermal conduction. In the crystalline crust, a first-order calculation can be obtained by a steady-state approach (e.g. Turcotte and Schubert, 2002), described by the following equation:

$$H = \nabla(\lambda_b \nabla T) \qquad \text{Eq. (1)}$$

where H is the radiogenic heat production, ∇ is the nabla operator, and λ_b the bulk thermal conductivity. The steady-state 3D thermal field is computed using a numerical model scheme based on the finite element method with the software GOLEM (see details in Cacace & Jacquey, 2017). We used the uppermost 75 km of the 3D data-constrained structural and density model by Gómez-García et al. (2020, 2021) (Fig. 2a) as the main input, where dominant lithologies were assigned to individual layers. In the computed thermal field (Fig. 2b), the heat transport within the lithosphere depends on the temperatures used as boundary conditions (Fig. 2c and 2d) and on the thermal properties of each lithospheric layer (H and λ_b), whose values were assigned as explained hereafter.
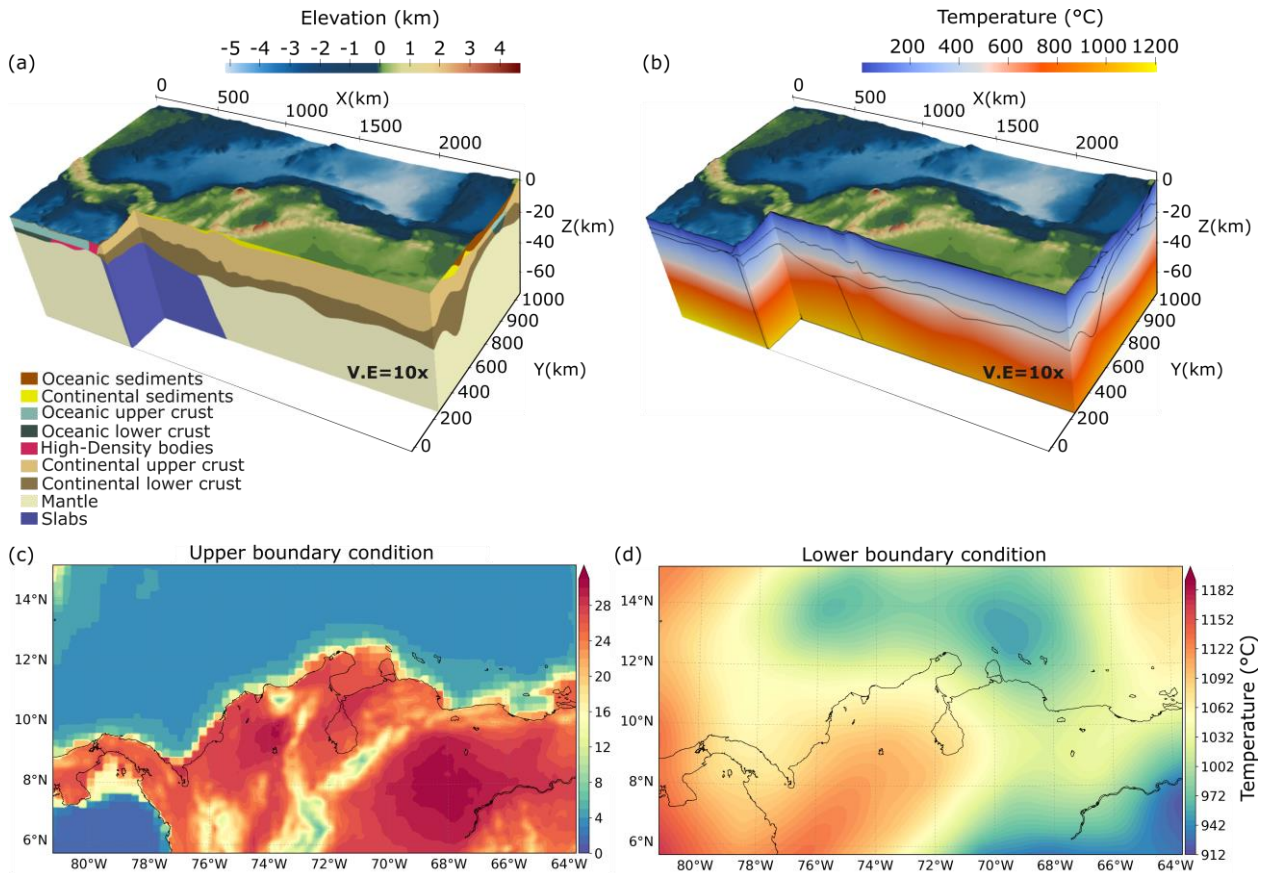
Figure 2. The thermal calculation was based on a 3D data-integrative model of the study area, which includes the thermal signature of the heterogeneities from the upper mantle (75 km depth) to the surface. (a) 3D structural model (Gómez-García et al., 2020, 2021) used to compute the 3D thermal field. The model includes fifteen different layers, but the figure only depicts those visible in the 3D view. (b) 3D steady-state thermal calculation, which integrates the complexity of the different layers within the structural model. Lithology-constrained thermal parameters were assigned to each of them (Table 1). Both the structural and thermal models are shown with a 10X vertical exaggeration. (c) Upper boundary condition integrating temperatures over the continent from the ERA5-Land dataset (Muñoz Sabater, 2019), and on the seabed from the GLORYS dataset (Ferry et al., 2010). (d) Lower boundary condition set as the temperatures at 75 km depth, after converting S-wave velocities into temperatures (details in Sect. 3.1.2).

3.1.1 Lithospheric structural model and definition of thermal properties

The data-constrained structural and density model of the South Caribbean margin (as detailed in Gómez-García et al., 2020, 2021) (Fig. 2a) represents the complexity of the Caribbean realms by including fifteen different layers (Table 1). Aiming

to have a detailed spatial resolution for the thermal calculations, the structural model was here refined to a 5 km x 5 km horizontal cell size.

The density of each layer, as constrained by 3D gravity modelling (Gómez-García et al., 2021) helps constraining its main lithology, and in turn, thermal properties such as thermal conductivity and radiogenic heat production can be assigned to each of them (e.g.: Ehlers, 2005; Hasterok et al., 2018; Vilà et al., 2010). The supplementary material (Text S1) details how the thermal conductivities and radiogenic heat production were determined, as well as the sensitivity analysis of the thermal properties (Text S2). In this sensitivity test, we explored the response of 25 different models taking into account a range of feasible thermal values for some of the modelled layers. Table 1 summarizes the lithologies inferred for each layer (which are compatible with derived densities and with the geologic and tectonic setting of the Caribbean), the final thermal properties used for the modelling, and the rationale behind each choice.

3.1.2 Upper and lower boundary conditions

The thermal upper boundary condition (Fig. 2c) was derived by integrating the average onshore surface temperatures from the ERA5-Land dataset, from January 2015 to April 2019 (Muñoz Sabater, 2019), and the average temperatures at the seafloor from GLORYS reanalysis (Ferry et al., 2010) for the year 2015. In the modelled domain, the integrated temperature field ranges from ~1°C in the Pacific Ocean to a maximum of ~30°C over Venezuelan territory. As expected, the temperatures over the mountains are the lowest of the continental realm, with an average of ~8°C for the period used in this research.

The temperature field at 75 km depth was defined as the lower boundary condition (Fig 2d). It was calculated from a conversion of the S-wave velocities from the SL2013sv tomographic model (Schaeffer and Lebedev, 2013) to temperatures, following the approaches of Goes et al. (2000) and Meeßen (2017) and the composition shown in Table S3. This thermal boundary depicts two cold domains: the Guyana shield, with minimum temperatures of ~912°C, and within the Caribbean region, with a mean value of ~972°C. In contrasts, the region where the Nazca and Caribbean flat slabs are present is hotter than the surroundings, reaching up to ~1100°C. All lateral borders of the model are assumed to be closed.

Table 1. Thermal properties defined for each lithospheric layer. Densities from Gómez-García et al. (2021). λ_b: Bulk thermal conductivity. H: Radiogenic heat production. C-LIP: Caribbean Large Igneous Plateau. See details in Text S1 and S2.

Layer	Density (kg m⁻³)	λ_b (W m⁻¹ K⁻¹)	H (μW m⁻³)	Rationale for λ_b	Reference for H
Oceanic sediments	2350	2.55	1.1	Average between sandstone, limestone and shale[a]	Mean value for sedimentary rocks[b]
Continental sediments	2500	3.5	1.19	Assuming sandstones[a]	Mean value for detritic sedimentary rocks[b]
Oceanic upper crust	3000	2.1	0.358	Mean value for basalts[a]	Mean value for basalts[b]
Low density bodies (Aves Ridge)	2900	2.6	1.07	Average for basalts and granites[a] following the composition by[c]	Eq. S1, using the average concentration of U, Th and K for Aves Ridge samples[c]
High density bodies in the upper oceanic crust	3250	2.93	0.057	Average for basalts, gabbros and peridotites[a] assuming a C-LIP mixed composition	Eq. S1, using the average concentration of U, Th and K for C-LIP samples[d]
Oceanic lower crust	3100	2.95	0.468	Mean value for gabbros[a]	Mean value for gabbros[b]
Low density bodies in the lower oceanic crust (Aves Ridge)	3000	2.6	1.07	Average for basalts and granites[a] following the composition by[c]	Aves Ridge samples[c]
High density bodies in the lower oceanic crust	3250	2.93	0.057	Average for basalts, gabbros and peridotites[a] assuming a C-LIP mixed composition	Eq. S1, using the average concentration of U, Th and K for C-LIP samples[d]

Continental upper crust	2750	2.4	0.6	Assuming a granitic composition[a]	Assuming a granitic composition[b]
Low density bodies in the upper continental crust	2600 - 2650	2.1	0.4	Assuming a basaltic composition[a]	Assuming a basaltic composition[b]
High density body in the upper continental crust (Santa Marta massif)	3000	2.95	0.667	Mean value for gabbros[a]	Assuming a gabroic composition[b]
Continental lower crust	3070	2.4	0.5	Assuming a granitic composition[a]	Assuming a granitic composition[b]
High density subcrustal bodies	3242	4.15	0.01	Mean value for dunites[a] assuming a depleted, high-density mantle material	Value for depleted peridotites[b]
Slab	3163	3.3	0.001	Assuming a prevalence of peridotites[a]	Eq. S1, using the average concentration of U, Th and K reported for depleted mantle[a]
Lithospheric mantle	3D solution	3	0.012	Assuming a peridotitic composition[a]	Eq. S1, using the average concentration of U, Th and K reported for mantle[a]

[a]Turcotte & Schubert (2002), [b]Vilà et al. (2010), [c]Neill et al. (2011), [d]Kerr (2014), [e]Montes et al. (2019).

3.1.3 Validation of the modelled temperatures

180   The calculated 3D thermal field was validated by comparing measurements available from downhole temperatures (ANH, 2020) and surface heat flow (Lucazeau, 2019) with the corresponding modelled values. Control point locations are shown in Fig. 3. Only the heat flow observations with the highest qualities (error range between 10% and 20%) were considered. In general, the measured heat flow is lower within the Caribbean Sea (40-80 mW m^{-2}) than in the Pacific Ocean (>80 mW m^{-2}). Minima (10-40 mW m^{-2}) are found close to the area of influence of the

185   Magdalena Fan depocenter (MFD, Fig. 3), likely as a result of the thermal blanketing by the thick sedimentary sequence (Scheck-Wenderoth and Maystrenko, 2013).

3.1.4 Geothermal gradient

    The geothermal gradient (∇T) was computed considering the modelled temperature ($T_{i,j}$) at different depth levels ($z_{i,j}$), following Eq. 2. As the geothermal gradient is not constant with depth, we explored its variation for

190   depths ranging from the surface (z=0) down to z=30 km, with incremental steps of 3 km. Moreover, the geothermal gradient for the crustal seismogenic zone was computed as the temperature difference between the surface and 20 km depth.

$$\nabla T(z) = \frac{T_i - T_j}{z_i - z_j} \qquad\qquad \text{Eq. (2)}$$

    A similar approach was followed by Gholamrezaie et al. (2018), and it allows to justify the use of a 3D

195   modelling scheme in which the geological heterogeneities of the system are included. This is particularly useful in complex tectonic settings such as the study area, where the assumption of a 1D geotherm approach will not be representative of the present-day configuration.
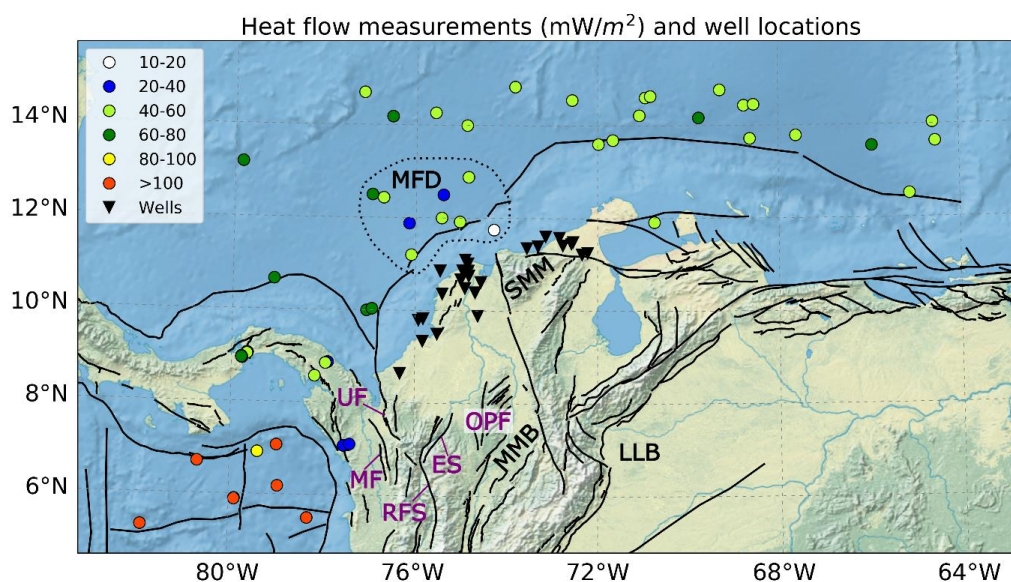
Figure 3. Measurements used for validating the thermal model. Color-coded dots: heat flow measurements with the

200 highest qualities (Lucazeau, 2019). Black triangles: wells from the oil industry with measured downhole temperatures

(ANH, 2020). Active fault traces (black lines) as in Fig. 1. ES = Espíritu Santo Fault. OPF = Otú-Palestina Fault system. RFS = Romeral Fault System. MF = Murindó Fault. UF = Uramita Fault. The dotted polygon highlights the heat flow measurements close to the Magdalena Fan depocenter (MFD). Additional features discussed in the text: LLB = Llanos Basin. MMB = Middle Magdalena Basin. SMM = Santa Marta Massif.

205   **3.2 Crustal seismogenic thickness**

The depths of the upper and lower stability transitions for seismogenesis, and the crustal seismogenic thickness (given by their difference) were calculated from the earthquake catalogue, as described below.

3.2.1 Earthquake catalogue

Since the study area covers several countries, a global earthquake catalogue was preferred over national ones.
210   We therefore relied upon the reviewed ISC Bulletin (International Seismological Centre, 2022), regarded as the definitive record of the Earth's seismicity. This catalogue has been completely rebuilt for the period 1964-2010 (Storchak et al., 2020), adding additional earthquakes and relocating hypocenters with the same location procedures used from 2011 onwards (Bondár and Storchak, 2011). However, for earthquakes occurring before 1980, the ISC Bulletin is still particularly heterogeneous (e.g.: Woessner & Wiemer, 2005). Consequently, we limit our study to the
215   period since 1980. Only prime hypocenters (i.e.: those relocated, or considered as best determined by ISC, see Di Giacomo & Storchak, 2016) were used. At the time of this analysis, the bulletin had been reviewed until March 2020.

The ISC Bulletin frequently reports several magnitudes for each event. We chose only those associated with the prime hypocenter, and adopted the hierarchy proposed by ISC for selecting the most reliable, preferred magnitude type (Di Giacomo and Storchak, 2016) (see supplementary material for details). Earthquakes without reported
220   magnitudes were disregarded.

The catalogue was analyzed in details (see the supplementary materials), considering the time series of magnitude values (e.g.: Gentili et al., 2011; González, 2017) and a sudden improvement of regional seismic monitoring in June 1993 (Arcila et al., 2020). The latter was used to divide the catalogue into two sub-periods with different mean magnitude of completeness (calculated with the maximum curvature method, Wiemer & Wyss, 2000, Woessner &
225   Wiemer, 2005): M_c = 4.6 from January 1980 to May 1993, and M_c = 3.5 from June 1993 – March 2020. These magnitude values were used as minimum thresholds for the subsequent analysis.

Earthquakes with non- reported depths, as well as those with depths reported as 0 km or fixed, or with reported depth error > 30 km were also excluded from the analysis of hypocentral temperature determinations. This selection allowed pruning the worst located earthquakes but preserving a sufficient number of events to perform our analysis.
230   Note that the hypocentral depth errors reported in the ISC Bulletin format are wide, since they cover the 90% uncertainty range (Biegalski et al., 1999). The possible impact of the remaining hypocentral depth uncertainties on the results will be commented on later.

The reference surface used as depth=0 in the ISC Bulletin is the WGS84 reference ellipsoid (István Bóndar & Dimitri Storchak, pers. comm., 2020; see also Bondár & Storchak, 2011). Our thermal model considers the actual
235   depth below sea level as reference, so hypocentral depths were referred to the EGM2008-5 geoid model (Pavlis et al., 2012). After this correction, earthquakes located above the solid Earth's surface (within the ocean water column or the atmosphere, according to the GEBCO topographic model, Weatherall et al., 2015) were excluded from our analysis. Such mislocations are the unfortunate consequence of disregarding the actual Earth's topography and bathymetry in the majority of the routine hypocentral depth determinations by ISC (and most seismological agencies).
240   This location problem is emphasized in study areas such as ours, with several kilometers of topographic relief between the ocean bottom and the mountain tops.

Since we focus our analysis on crustal seismicity, we also disregarded earthquakes located below the crust-mantle (Moho) boundary, as provided by the GEMMA model (Reguzzoni and Sampietro, 2015), interpolated to a homogeneous grid of 5 km × 5 km. We preferred the GEMMA model over other models available in the region (e.g.:

245 Avellaneda-Jiménez et al., 2022; Poveda et al., 2018) because either these studies do not cover the entire study area, or portray large regions with data gaps, as they relied on available seismic stations. The remaining subset thus only contains the best located, crustal earthquakes in the region (Fig. 1), which will be the ones used for calculating the upper and lower stability transitions (Sect. 3.2.2) and hypocentral temperatures (Sect. 4.2).

250 The scalar seismic moment (M_0, in N·m) was calculated for this subset, from the standard IASPEI formula for the moment magnitude M_w (see Bormann, 2015 after Kanamori, 1977). If the preferred magnitude from the ISC Bulletin was not already M_w, it was first converted to it using relations detailed in the supplementary materials (Text S6): Di Giacomo et al. (2015, exponential versions, for body-wave or surface-wave magnitudes), Arcila et al. (2020, for local magnitudes) and (Salazar et al., 2013, for duration magnitudes).

255 The data repository (Gomez-Garcia et al., 2022) provides the analyzed earthquake subset, with their preferred magnitudes, estimated M_0 and calculated hypocentral temperatures.

3.2.2 Upper and lower stability transitions and uncertainty quantification

The 10% and 90% depth percentiles (D10 and D90, respectively; Marone & Scholz, 1988; Sibson, 1982) were spatially mapped considering the subset of crustal earthquakes with the best hypocentral depth determinations (see previous section). We used the median-unbiased percentile estimator of Hyndman & Fan (1996) at each node of
260 a latitude-longitude grid with a spacing of 0.1°, considering the 20 closest earthquakes to each node as the sample for calculating the corresponding D10 and D90 values, provided that these events were at a maximum distance of 120 km from the node. To avoid boundary effects, we considered earthquakes outside the study area, applying the same selection procedure, after checking that M_c was not larger in this extended region (with a buffer of 120 km).

Although this way of spatial sampling of a fixed number of the closest earthquakes is novel for calculating
265 hypocentral depth percentiles, it has been frequently used for mapping M_c and b-values of the Gutenberg-Richter distribution (firstly by Wiemer & Wyss, 1997). The reason for our choice is that it maximizes the mapping detail, that is, the resolution radius (epicentral distance to the 20th closest earthquake from the node in our case) will be small in locations with high spatial earthquake density, and large in locations with sparse seismicity. The upper threshold of this radius was chosen by inspection of the resulting maps, to avoid calculating D10 and D90 in regions where the
270 spatial density of epicentres was too low to obtain reliable results. Further details of the resulting map resolution will be commented on in Sect. 4.4.

For each node, 10000 random bootstrap samples (Efron, 1979) were generated out of the corresponding 20 best estimates of the hypocentral depth values, and from them the average D10 and D90 values and their respective bootstrap standard deviations were calculated. Considering all nodes with percentile determinations, the mean
275 standard deviation was 0.4 and 0.8 km, and the maximum one was 1.8 and 4.3 km, for D10 and D90 respectively (see histogram of standard deviations in Fig. S6). These low uncertainties indicate that using 20 earthquakes for each node is already reliable in our case to obtain stable D10 and D90 values. Indeed, samples with as few as 20 earthquakes for calculating D90 were used, e.g. by Chiarabba and De Gori (2016). Using a larger earthquake sample for each node was avoided, as it would imply enlarging the resolution radius, considering earthquakes located further away from the
280 nodes, and thus smoothing out the spatial variations of D10 and D90.

The temperatures at the depths of D10 and D90 at each node of the map were calculated from the 3D thermal model. Due to the sampling method used for determining D10 and D90, in most nodes of the map the calculated D10 and D90 lie within the crust, but there are some in which the percentiles may be located above or below the crust, respectively (i.e.: in regions with abrupt topography/bathymetry or Moho interface). In either case, those nodes lying
285 outside the bounds of our structural model were not considered. The resulting D10 and D90 values, and their corresponding standard deviations are provided in the data repository (Gomez-Garcia et al., 2022).

4 Results and discussion

4.1 Thermal model validation

In Fig. 4a we compare the modelled and measured temperatures at different boreholes (see Fig. 3), based on the selected, best fitting thermal model resulting from the sensitivity test (Text S2). In general, there is a good agreement between the modelled temperatures (cyan dots) and the observed ones (black dots). The histogram of residuals (Fig. 4a, right) indicates that most misfits range between -10 and 10°C, with a mean of 4.99°C; although larger misfits occur at shallower depths (< 1km). Such a trend could be explained by shallow advective processes of heat transport (e.g., by groundwater), which have not been considered in our model.

The modelled heat flow is generally lower than the measurements, except in the area of influence of the Magdalena Fan (Fig. 4b). The heat flow data in the Pacific Ocean are located in an area of intense faulting (Marcaillou et al., 2006), close to the Panama Fracture Zone; therefore, additional advective heat transport might be responsible for the high measured heat flow values in this region. Considering that the associated error in the heat flow data used in this analysis ranges between 10 and 20% (Lucazeau, 2019), it is possible to conclude that the model fits the regional trend, except in those two areas previously mentioned. Nevertheless, the heat flow data is usually affected by nonconductive processes, such as hydrothermal circulation. For this reason, their interpretation in terms of a purely conductive, lithospheric-scale model is difficult, as other authors have pointed out (Klitzke et al., 2016; Scheck-Wenderoth and Maystrenko, 2013).

4.2 The need of a 3D thermal approach

To rely on a multi-1D approach, as commonly done, to compute the thermal field implies a homogeneous geological setting where lateral variations in the heat fluxes, as they do naturally occur, are disregarded. Some implications of oversimplifying such three-dimensional interactions via 1D and 2D model representations have been already discussed for instance by Cacace and Scheck-Wenderoth (2016). The thermal field within the lithosphere is influenced by a variety of factors such as: 1) the imprint from deep mantle sources; 2) the heat produced by the radioactive decay of elements present in the crystalline crust; 3) the thickness of sedimentary depocenters; and 4) the geometries of the different layers that compose the lithosphere. It is therefore likely that a 3D thermal approach can better resolve all those interactions while also preserving the heterogeneous subsurface configuration.

In particular, regional geothermal gradient variations can provide insights about the thermal state of the lithosphere (e.g.: Gholamrezaie et al., 2018). Figure 5a shows the computed geothermal gradient for the regional seismogenic zone (from the surface down to 20 km depth), with the temperatures extracted from the 3D thermal model. Long wavelength spatial variations are observed both in the oceanic and continental realms, with minima offshore (13°C km^{-1}) and maxima underneath the Colombian Andes (up to 23°C km^{-1}). Figure 5a also depicts how the selected crustal earthquakes (International Seismological Centre, 2022) occur in tectonic environments with a diverse range of geothermal gradients. This again is an indication that a 1D approximation is not robust enough to model the thermal configuration of the study area.

Moreover, the geothermal gradients can also be used as an indirect indicator of crustal rheology. In Fig. 5a, it is possible to observe the correlation between the spatial distribution of seismicity and the geothermal gradients in this region. Most of the seismicity preferentially clusters around zones with geothermal gradients > 19 °C/km^{-1}, i.e. in the North Andes terranes and Panama microplate. Such a correlation indirectly suggests that the latter are places where the crust and lithospheric mantle are strongly coupled, and therefore, the differential stress does not exceed the static crustal strength.

A quantitative measure of the correlation between the spatial distribution of seismicity and the geothermal gradients can be made with the so-called Molchan (or error) diagram (Molchan, 1990, 1991; Molchan and Kagan, 1992, Fig. 5b), already used to test the skill of geodynamic variables at forecasting the spatial distribution of seismicity (e.g.: Becker et al., 2015).
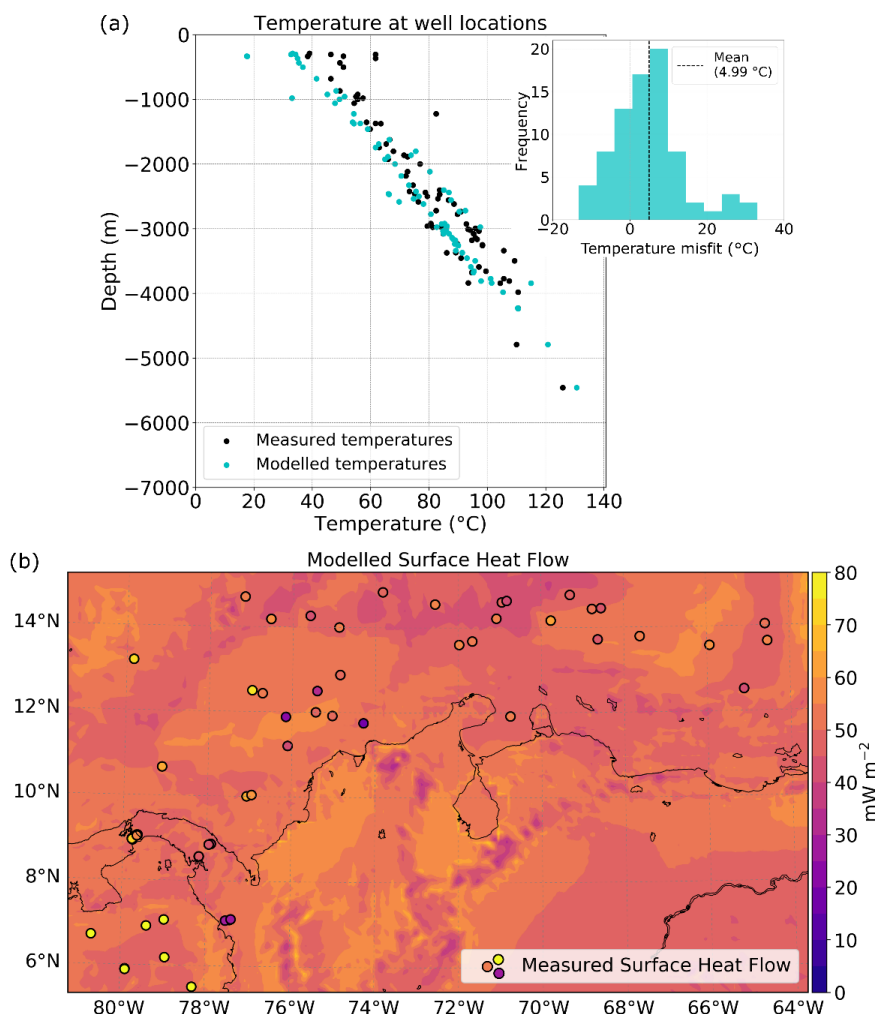
335

Figure 4. Validation of the 3D thermal field against measurements of downhole temperatures and surface heat flow. (a) Modelled temperatures show a good agreement with the observed temperatures. The largest misfits (histogram of the right panel) occur at depths shallower than 1km. (b) Calculated surface heat flow (background) and measured values (colored dots, with the same color bar).

340

       In a map with a continuous 2-D function (like the geothermal gradient in Fig. 5a), the Molchan diagram (blue curve, Fig. 5b) is a plot of the fraction of missed events versus the fraction of geographic area of the map (Zechar and Jordan, 2008). Each point of the diagram corresponds to a different threshold of the geothermal gradient. At and above this threshold, there is a fraction of the geographic map area (i.e. fraction of occupied space), and a fraction of

345 earthquakes occurred in those locations, i.e. they are forecast at that threshold. The remaining earthquakes, which occurred elsewhere (at locations were the geothermal gradient is lower), are not forecast at this threshold, so they are the fraction of missed earthquakes.

A purely random guess with no skill would yield a curve close to the diagonal shown as a dashed line in Fig. 5b. A skilful correlation (or forecast) would yield a curve below this diagonal, with larger departures being more statistically significant (Zechar and Jordan, 2008). Fig. 5a contains *N*=1404 crustal earthquakes with well-determined depth (according to the criteria described in sect. 3.2), and for such a number, the departure of the curve is statistically significant (Zechar and Jordan, 2008). This test is physically meaningful, given that no seismicity information was used for calculating the geothermal gradients or vice versa.

The observed correlation between seismicity and geothermal gradient is not a direct one, but the conclusion that is meaningful is strengthened by the fact that regions with very low calculated geothermal gradient (below 15.85°C km^{-1}, which occupy 16% of the map area) are devoid of crustal earthquakes (Fig. 5a), resulting in a miss rate equal to zero already for a fraction of 84% of occupied space in the map (Fig. 5b).

The area above the curve can be used as an overall measure of the skill (Zechar and Jordan, 2008). In particular, the score *S* (Becker et al., 2015) is the area above the Molchan diagram minus 0.5. This exercise with the calculated geothermal gradient yields *S*=0.249. Albeit the results from different geographic regions cannot be directly compared, this value is very similar to those of the most skillful geodynamic variables (i.e.: shear strain rates and rates of topography change) tested in western North America by Becker et al. (2015). Therefore, our results indicate that the geothermal gradient has significant skill at forecasting the spatial distribution of seismicity in the study area.

As the geothermal gradient is a function of the temperatures at given depths (Eq. 2), it changes according to the depth interval used for its calculation; therefore, we explored its variation considering depth intervals of 3 km, from the surface down to 30 km depth (Fig. S2). Besides a general decrease in the geothermal gradient with depth, the most remarkable results are that for the continental realm, there is not a constant pattern at all depths. In the elevated Andes mountains, the geothermal gradient is high in the uppermost 6 km (Figs. S2a and S2b), but this trend shifts at larger depths, where the highest gradients spatially correlate with thick sedimentary depocenters (Fig. S3). This behavior is consistent with an increase in the amout of radiogenic heat production associated with the thick crystalline crust of the Andes, and the thermal blanketing effect of the sediments, which retain heat in the underlying crust (Cacace and Scheck-Wenderoth, 2016; Scheck-Wenderoth and Maystrenko, 2013).
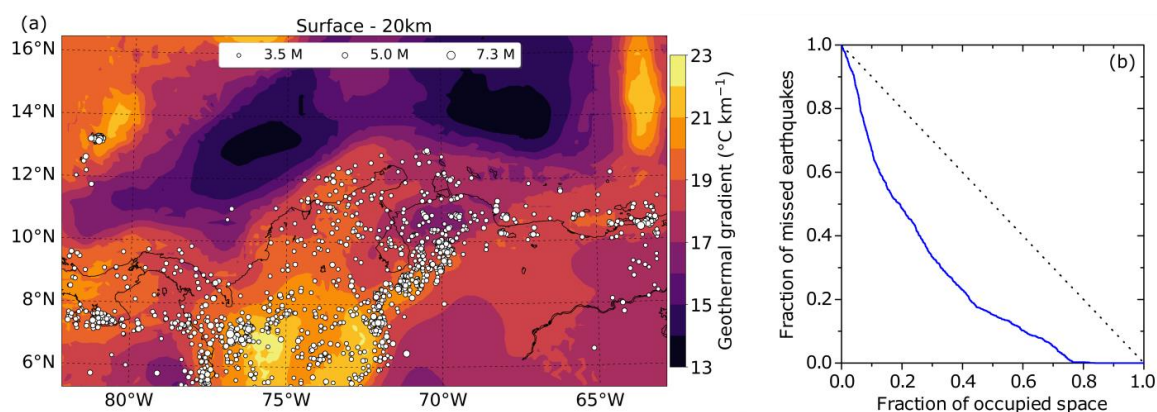
Figure 5. Correlation between geothermal gradient and the spatial distribution of crustal seismicity. (a) Geothermal gradient in the study area computed in the uppermost 20 km of the lithosphere (about the regional average depth of the lower crustal stability transition of seismogenesis, Sec. 4.3). Large spatial variations are observed both onshore and offshore. White dots: Crustal seismicity analyzed in this study (International Seismological Centre, 2022), selected as detailed in Sec. 3.2.1. (b) Molchan diagram showing the skill of the spatial variations in the geothermal gradient at forecasting the distribution of crustal earthquakes. The dashed diagonal would be the expected result of a random prediction, and a skillful forecast should yield a curve below it.

4.3 Relation between lithology, hypocentral temperature and seismic moment release

385   The modelled hypocentral temperature distribution of the selected earthquake dataset is shown in Fig. 6. We will focus our discussion around the three sub-regions as previously defined in Fig. 1.

        Seismicity is frequent in region 1, as it hosts the Murindó seismic cluster, including the largest earthquake of the selected dataset (M_s = 7.3), with a hypocentral depth of 16.7 km (Fig. 1), and an associated modelled temperature of ~375°C. In the Otú-Palestina and El Espíritu Santo fault systems (region 2) the deepest hypocentral depths are
390   reported (> 30 km) (Fig. 1), giving as a result modelled hypocentral temperatures of more than 600°C. In the Venezuelan Andes, bounded by the Boconó fault (region 3) seismicity is spatially denser than in the rest of the North Andes terranes, and shows a shallowing pattern from the southwest towards the northeast (Fig. 2). Such a trend implies a transition from hotter hypocentral temperatures close to the Colombian-Venezuelan border towards colder ones in the Falcon basin.

395   A synthesis of modelled temperatures for the entire study area is presented in Fig. 7. Figure 7b also depicts the seismogenic window typically associated with granite (90-350°C), gabbro (200-600°C) and olivine gouge (600-1000°C), according to the review presented by Scholz (2019). Granitic rocks are typically regarded as the representative lithology in the crystalline continental crust. However, the study area has a variety of allochthonous terranes that have been attached to the margin, including large ophiolite sequences, associated to oceanic plateaus,
400   and magmatic arcs (Montes et al., 2019); therefore, the seismogenic windows of gabbro and olivine were also considered.
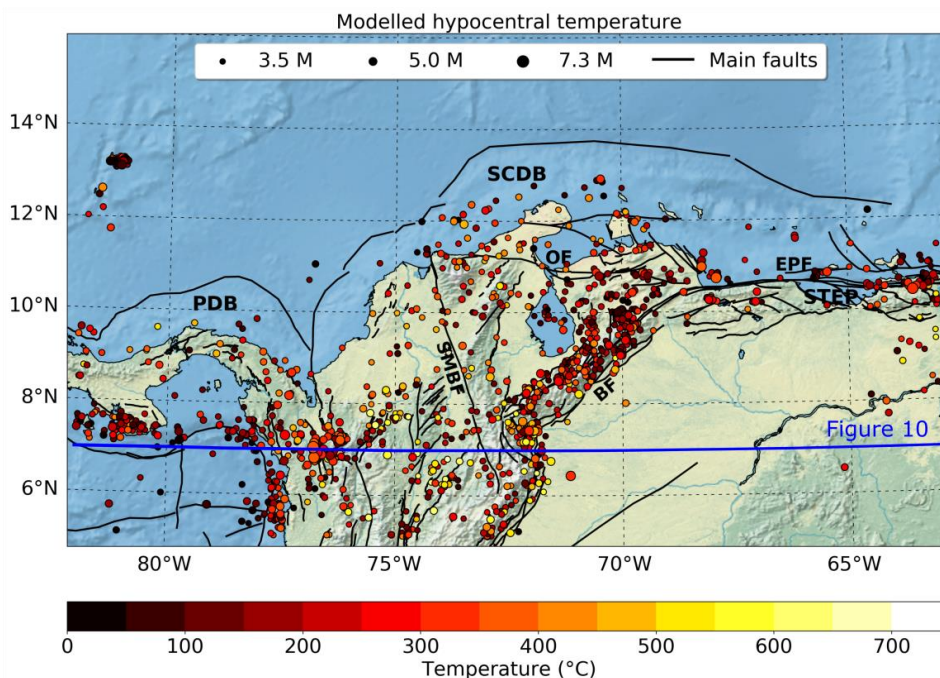
Figure 6. Modelled hypocentral temperature for crustal earthquakes. Acronyms and active fault traces (black lines) as in Fig. 1. The surface projection of the vertical profile of Fig. 10 is shown as a blue line.

405   The majority of the seismic events share hypocentral temperatures of less than 350°C (Fig. 7a), within the observed seismogenic window of granite and/or partially overlapping with that of gabbro (Fig. 7b). Nevertheless, modelled temperatures range from 1°C (offshore events) to almost 700°C, with only few events reaching the seismogenic window reported for olivine gouges at > 600°C. These ranges, however, are not strict because in nature rocks are a mix of different minerals that can contribute to a more complex behavior. For example, mixtures of 65% illite and 35% quartz might exhibit a seismogenic window between 250 and 400°C, while replacing the illite for muscovite implies a new window between 350 and 500°C (see grey dashed line in Fig. 7b) (Scholz, 2019 and references therein).

The hypocentral depths show a slightly bimodal distribution, with the largest peak between 0 and 5 km and a secondary one at ~10 km (Fig. 7c). Computing the D10 and D90 associated to the whole catalogue of selected crustal earthquakes results in a regional seismogenic zone ranging on average between 1.8 and 20.9 km. The occurrence of seismicity at very shallow depths (< 2km) suggests the presence of not well-developed faults in the study area (Scholz, 2019). However, despite relying only on the best located earthquakes (see Sect. 3.2.1), large errors in the hypocentral depths still remain (up to 30 km, see Fig. S5), and should be considered in the analysis of our results.

The largest events (*M* > 6.5) were recorded between 15 km and 20 km depth (dark blue dots in Fig. 7b), close to the lower stability transition (D90). This behavior supports early findings broadly debated in the literature (e.g.: Tse & Rice, 1986), and suggests that ruptures which initiated within deep and high-stress regions are able to propagate through the entire seismogenic zone and probably reach the surface, resulting in a large rupture area, and therefore, in a large magnitude event. In particular, our analysis indicates that this could have occurred in the Murindó sequence in 1992. The two largest events ($M_s = 7.3$ and $M_s = 6.8$) occurred at the base of the seismogenic zone (16.7 km and 15.5 km, respectively), and are dominating the seismic energy release content in the study area, as can be observed on the seismic moment release curve (Fig. 7d). The geological effects of the 18 October 1992 mainshock suggest that it probably caused surface rupture exceeding 100 km in length (Mosquera-Machado et al., 2009), compatible with the overall rupture length deduced from the source-time functions of the earthquake sub-events (Li and Toksoz, 1993) and the size of the aftershock distribution (Arvidsson et al., 2002). Thus, we infer that the mainshock ruptured the whole seismogenic crust, from its base up to the surface.

4.4 Depths and temperatures at the upper and lower stability transitions (D10 and D90)

The maps of D10, D90 and their temperatures, shown in Fig. 8, evidence spatial variations whose limits can sometimes be traced to known crustal structures. Several patterns can be recognized regarding the computed upper stability transition (D10, Fig. 8a). Close to the Murindó cluster (region 1), the Uramita fault acts as a preferential boundary between deeper the D10 values in the Panamá-Chocó block, and shallower ones to the east of the fault, in the northern part of the Western Cordillera. In region 2, D10 reaches a local maximum of almost 10 km depth in the Otú-Palestina system. The Venezuelan Andes (region 3) are characterized by relatively homogeneous, shallow values of D10 of less than 2 km. The Oca-Ancon fault systems bound deep D10 values towards the north of the fault, and shallow values towards the south.

The most remarkable patterns found about the lower stability transition (D90, Fig. 8b) are its deep values associated to the Otú-Palestina and El Espíritu Santo fault systems (region 2). D90 depths of almost 35 km in the Otú-Palestina are in agreement with the crustal-scale structure that these systems likely represent (Kennan and Pindell, 2009) and are consistent with significant rheological contrasts in the transition between the Central and Eastern Cordilleras. The D90 values in the Venezuelan Andes are clearly bounded by the presence of major faults, reaching shallow depths, up to 8 km. However, the signal of the Uramita and Oca-Ancon faults acting as a boundary of terranes as previously discussed per the D10 is not present in the D90 map.
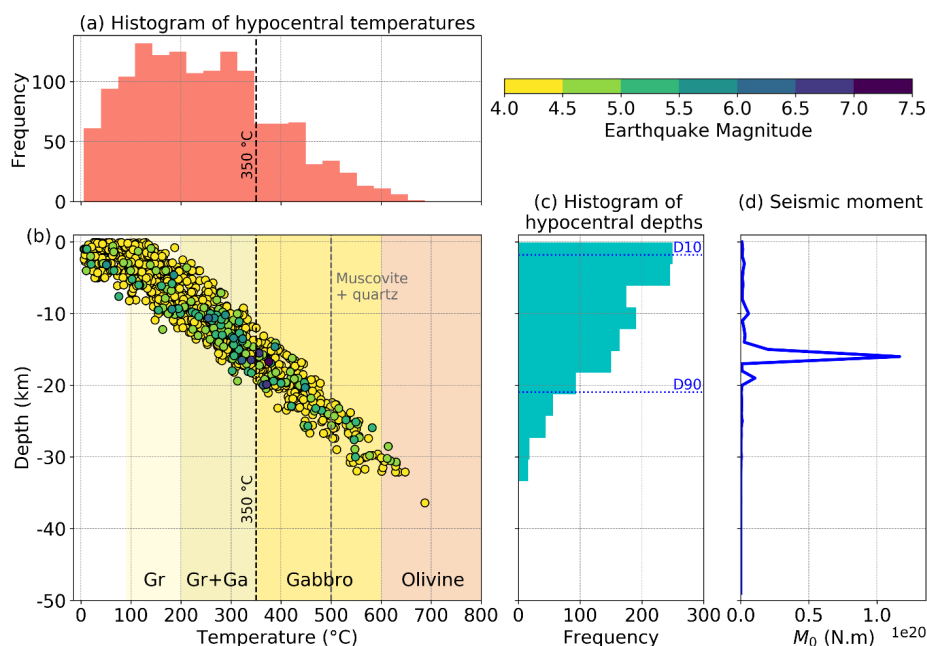
Figure 7. Synthesis of the modelled hypocentral temperatures. (a) Histogram of hypocentral temperatures. (b) Modelled temperature versus depth and preferred magnitude. Different colored domains represent the seismogenic window of different rocks or minerals as reported by laboratory experiments (Scholz, 2019). Gr = Granite. Gr+Ga = shared seismogenic window between granite and gabbro. (c) Histogram of hypocentral depths with regional D10 = 1.8 km and D90 = 20.9 km. (d) Histogram of seismic moment release (M_0, in N·m) as a function of depth, with depth bins of 1 km.

The temperatures along the D10 surface (Fig. 8c) are highly influenced by a topographic effect. Their maximum values correlate spatially to elevated mountainous areas in the Andes and the Santa Marta massif (SMM, Fig. 3), with a few exceptions north of the Oca-Ancon fault. The temperatures along the D90 surface (Fig. 8d), on the other hand, do not depict such strong correlation with topography. Instead, the hottest domains are associated to sedimentary basins (Fig. S3) and correspond to the deepest values of D90, i.e.: underneath the Otú-Palestina and El Espíritu Santo fault systems (region 2), influenced by the Middle Magdalena basin (MMB, Fig. 3), and beneath the Eastern Venezuelan and the Llanos basins (LLB, Fig. 3).

Our results suggest that the LST in the continental realm occurs over a wide range of temperatures, and in most of the study area, with values larger than those reported as the onset of quartz plasticity (~300°C, Zielke et al., 2020) and in some cases larger than the temperature range consistent with ductile behaviour (350±100°C – see a detailed review by Chen et al., 2013). The D90 temperatures are also higher than the seismogenic window of rocks and mineral assemblies typically found in the continental crust (see Fig. 7 and Sect. 4.2).

Given our results above, we should also notice the following points: 1) there are still large uncertainties in the selected events used in this study (up to 30 km) that could strongly influence the resulting D10 and D90 values; 2) the best-located earthquake dataset has a relatively small number of events, limiting the spatial resolution of the seismogenic thickness calculation (as discussed further in Sect. 4.5); 3) the dataset includes aftershocks (as otherwise the number of events for analysis would be further reduced), which may nucleate at depths larger than the base of the background seismogenic zone (e.g.: Zielke et al., 2020), so the calculated D90 values may be affected by transient

deepening of the LST during aftershock sequences; 4) the diverse lithology of the allochthonous terranes accreted to NW South America includes ultramafic, olivine-rich rocks, and therefore, could generate seismicity at temperatures larger than the seismogenic windows of granites and gabbros; 5) a thick lower crust together with a relatively hot upper mantle could contribute to large hypocentral temperatures (Sect. 4.5); and, 6) it is necessary to have more control points within the continental region to constrain the thermal model, as a particular lithology may have a wide range of radiogenic heat production and thermal conductivity values (e.g.: Vilà et al., 2010).
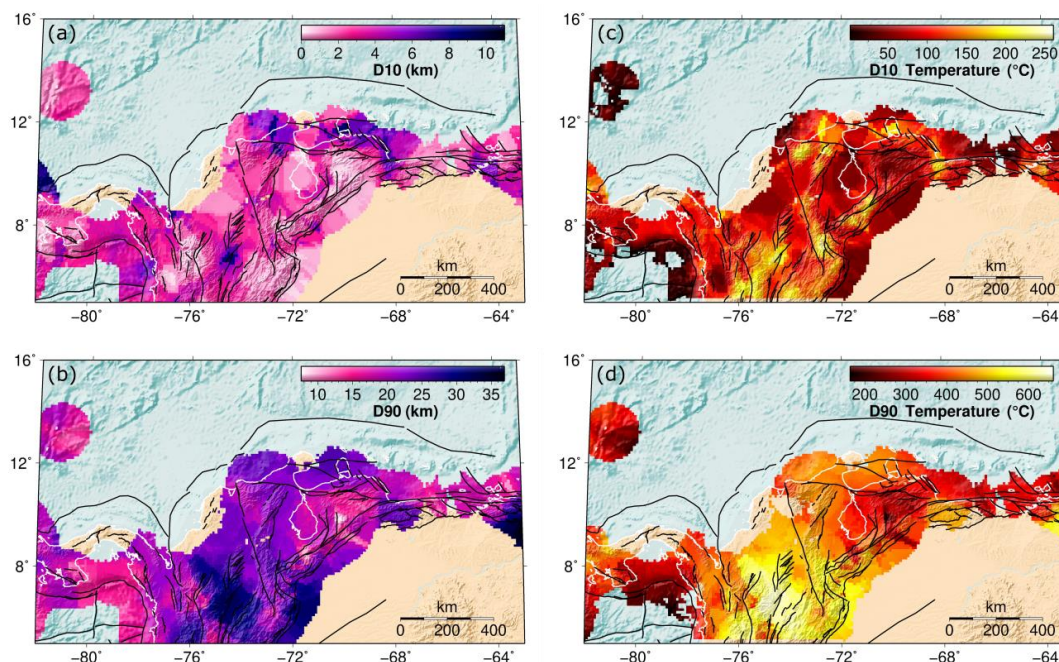
Figure 8. Depths and modelled temperatures of the upper (D10) and lower (D90) stability transitions for crustal seismicity. (a) D10. (b) D90. (c) D10 temperature. (d) D90 temperature. Black lines: active fault traces, as in Fig. 1. Coastlines are depicted as white lines.

4.5 Crustal seismogenic thickness

The crustal seismogenic thickness shows relatively large variations in the study area (Fig. 9a). Its minima (~7 km) are present in the Pacific Ocean offshore Panamá. A thin seismogenic crust is also observed along the Venezuelan Andes and offshore Venezuela, bounded by the Boconó and El Pilar fault systems. Higher seismogenic thicknesses (>30 km) are found in the Eastern Venezuelan basin and in the Otú-Palestina and El Espíritu Santo fault systems (region 2). We interpret these results in region 2 as indicative that the main faults in the area are well-developed crustal-scale structures, rather than shallow fault systems.

The reliability of these results (including both D10 and D90) highly depends on the density of earthquakes available for their calculation. This can be observed in the resolution radius map (Fig. 9b), which shows the search radius required for reaching 20 seismic events in the calculation of D10 and D90. As we allowed a maximum radius of 120 km, the map is truncated at this value. It is possible to observe how regions with dense seismicity required a small radius for reaching the 20 events, including the Murindó cluster (region 1) and the Venezuelan Andes (region 3).

The sources of error in the calculation of the CST are diverse, and include uncertainties in the Moho depths, as well as errors in the earthquake hypocentral depths. The errors associated with the Moho geometry (Fig. S8) are higher across the Nazca and South American realms, resulting in uncertainties about the location of the events either in the lithospheric mantle (including both the mantle wedge and the subducting slab), or in the lower continental crust.

500   Figure 10 shows a longitudinal profile along 7°N (see Fig. 6 for spatial location). Here it is possible to observe the thermal response of the system, considering the spatially heterogeneous lower boundary condition at 75 km depth. Underneath the Pacific Ocean, the 600°C isotherm bounds the majority of the seismic events located within the crust and uppermost mantle (black and grey dots), as previously suggested by Chen & Molnar (1983) and McKenzie et al. (2005), while the isotherm gradually shifts upward underneath western South America.
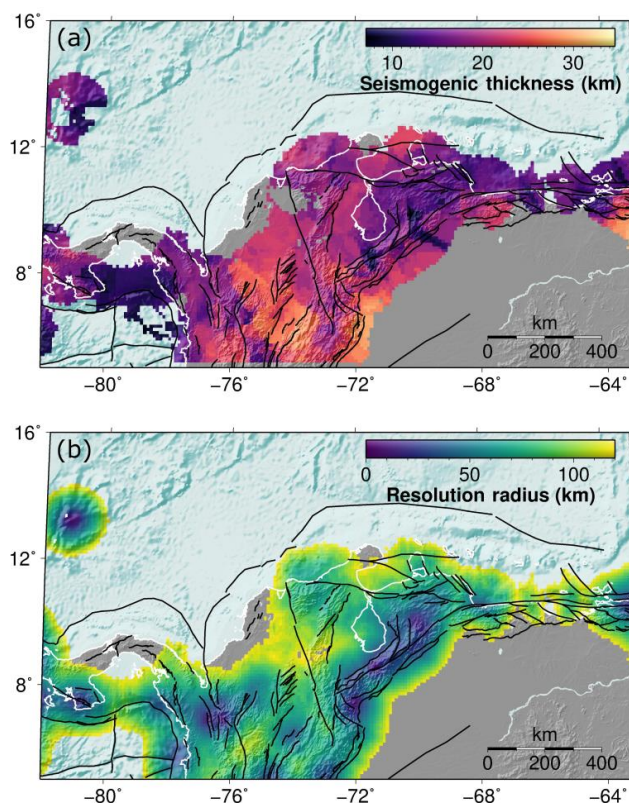
505

Figure 9. (a) Seismogenic thickness computed with the D10 and D90 values existing within the crust. (b) The resolution radius used to compute D10 and D90 shows high spatial variation and highlights regions with high and low density of seismic events. The maximum radius is 120 km. Black lines: active fault traces as in Fig. 1.

510   The thermal structure of the continental realm is usually more complex than that of the oceanic lithosphere. However, we observe a general trend between the lithospheric configuration and the seismicity distribution, that is the colder and therefore stronger the lithosphere, the deeper and higher in magnitudes the earthquakes (e.g.: Chen et al., 2013). Our results suggest that the lithospheric mantle underneath the Colombian Andes is hotter than the surroundings, as indicated by a shallowing of the 600°C isotherm (Fig. 10). As a response, most of the crustal seismicity there preferentially occurs at shallower depths. Nevertheless, deep events below the Moho interface (open

515   dots) are also present in this area, especially associated to the Coiba (Nazca) slab. Considering the uncertainties in the hypocentral depths, and also in the Moho estimates from the GEMMA model (up to ~7 km along this profile, Reguzzoni & Sampietro, 2015) it is especially challenging to make a clear statement about these upper mantle events. However we can hypothesize that the subducting Coiba plate can host such intraplate events. Similarly, the occurrence of upper mantle earthquakes is nowadays broadly recognized (e.g.: Chen et al., 2013) as also dehydration reactions
520   can trigger seismicity at temperatures above the normal BDT (e.g.: Rodriguez Piceda et al., 2022).

Two regions with prominent seismic activity at a crustal scale are recognized: the suture of the Panamá-Chocó block with NW South America, around the Murindó cluster; and close to the Guaicaramo and Yopal faults, the boundary between the North Andes terranes (Eastern cordillera) and the Guyana shield. As previously mentioned, most of the seismic activity in these areas is bounded by the 600°C isotherm. In these regions, the seismogenic
525   thickness and the depths to the upper and lower stability transitions do not show any direct spatial correlation with variations in Moho depth. However, the seismogenic crust is thicker and deeper where the largest depocenters are present, that is, beneath the Middle Magdalena (MMB) and the Llanos basins (LLB).

In particular, the abrupt deepening of D90 between ~74°W and 76°W spatially correlates with a thick lower crust and with a shallowing of the 600°C isotherm, suggesting that a mafic crust able to host deeper earthquakes
530   (deeper BDT) together with a hot upper mantle could contribute to the the observed increase in hypocentral temperatures in region 2, underneath the MMB. The main shock of the Murindó sequence in 1992 is depicted with a magenta star, and its proximity to the base of the seismogenic crust (D90) is evident.
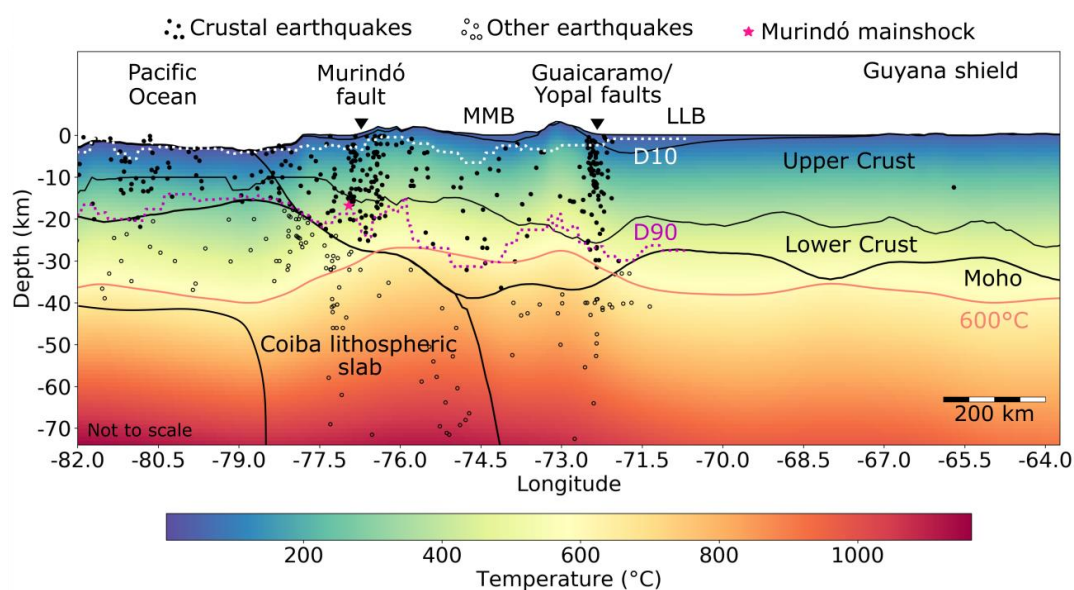
Figure 10. W-E profile at 7°N (see location in Fig. 6) showing the modelled temperatures and their relation to the
535   lithospheric structure, topography and seismicity. Vertical scale exaggerated. Black lines: Boundaries of the lithospheric layers of the structural model as integrated by Gómez-García et al. (2020, 2021). Pink continuous line: 600°C isotherm. Dotted lines: Depths to the upper and lower stability transitions (white: D10 and magenta: D90, respectively). Black filled dots: Crustal earthquakes used in this study. Open dots: Earthquakes deeper than the Moho interface, not used for calculating D10 or D90. The earthquakes projected in the profile include those from 6.5°N to
540   7.5°N. Star: Hypocenter of the largest earthquake (Murindó mainshock). LLB = Llanos Basin. MMB = Middle Magdalena Basin (which spatially corresponds to region 2).

5 Summary and conclusions

We have mapped the depth to the upper (D10) and lower (D90) earthquake stability transitions, and the CST in NW South America, considering only crustal seismicity. This approach allows focusing on the seismogenic properties of the crust, with a sampling procedure which allows identifying variations with greater detail in areas with higher spatial earthquake density. Some of those variations are shown to correlate with crustal-scale faults in the region, which consequently bound crustal domains with different seismogenic behaviors. Our calculations are limited by the completeness of the earthquake catalogue, and the precision of the hypocentral locations. They could be eventually refined in future analyses, as new seismic stations are installed and more earthquakes are being recorded, particularly of smaller magnitudes than those considered here ($M < 3.5$).

The presented three-dimensional approach for calculating of the thermal field allows retrieving spatial variations which would have been overlooked by simplified 1-D or 2-D models. Therefore, our workflow provides a good opportunity to compare limiting temperatures for seismogenesis provided by laboratory experiments against real-case scenarios, where the geological complexities are taken into account, including a realistic lithospheric structure and the mantle imprint into the crustal temperatures. Additional measurements of heat flow and borehole temperatures will eventually help constraining and validating the modelled temperatures. In particular, the study region has limited availability of those observables, and thus, the temperature estimates are also prone to uncertainties.

Most crustal seismic events in the study area have modelled hypocentral temperatures < 350°C, and are located at depths < 20 km. Although most of the hypocentral temperatures range in the reported seismogenic window of rocks and mineral assemblies typically found in continental crust, some of the deepest hypocenters have associated temperatures > 600°C, reaching the seismogenic window of olivine. Since diverse allochthonous crustal blocks have attached to the NW South American margin, including large ophiolite sequences, they may contain olivine-rich, ultramafic rocks able to host these earthquakes. Alternatively, these high-temperature events can be explained by either a thick, mafic lower crust, a hot upper mantle, large uncertainties of the Moho depths in the study area (up to 7 km), or by the still large errors associated to the hypocentral depths (up to 30 km), which could imply that those events actually occurred in the upper mantle.

The spatial variation in the geothermal gradient in the uppermost 20 km of the lithosphere has significant predictive power for forecasting the distribution of seismicity. Such a correlation had not previously been quantified elsewhere, to our knowledge, and similar tests would be worth performing in other regions in order to check if it is systematic.

Our results evidence that the ruptures of the two largest events that occurred in the region since 1980 ($M_s = 6.8$ and $M_s = 7.3$), pertaining to the Murindó sequence of 1992, propagated from the base of the seismogenic zone (lower stability transition). This highlights the importance of considering this transition for defining the lower boundary of seismogenic sources in seismic hazard assessments.

The estimated seismogenic thickness in the Otú-Palestina and El Espíritu Santo fault systems is one of the largest in the study area (up to ~30 km), as the deepest events have been recorded in these regions. This suggests that these fault systems likely behave as crustal-scale structures, which might have the potential of rupturing large fault areas, giving as a result large-magnitude, hazardous events.

Lastly, the seismogenic crust is thicker and hotter below the thick Middle Magdalena basin, suggesting that the thermal blanketing effect of the sedimentary cover (i.e., higher temperatures below sedimentary basins) may be able to affect the seismogenic behavior of the underlying crust.

Data availability

The results of this publication are available in the data repository Gómez-García et al. (2022). It includes the calculated 3D thermal model, the catalogue of selected earthquakes with their modelled hypocentral temperatures and seismic moment, and the mapped depths and temperatures of the upper and lower stability transitions (D10 and D90).

The thermal calculations were computed using the software GOLEM (Cacace and Jacquey, 2017) available at Jacquey & Cacace (2017). The figures were created using diverse Python packages (Python Software Foundation. Python Language Reference, version 2.7. Available at http://www.python.org) and GMT (Wessel & Smith, 1991).

Author contribution

AMG developed the research idea, processed the data, performed the thermal calculations and wrote the manuscript. AGG contributed to the research idea, processed the earthquake data and wrote the manuscript. MC developed the software GOLEM and provided support for the thermal calculations. MS and GM supervised the implementation of the thermal calculations. All authors contributed to the discussion and interpretation of the results, revised the manuscript and were partially responsible for obtaining the financial support to develop this research.

Competing interest

The authors declare that they have no conflict of interest.

Acknowledgments

AMGG was partially supported by grants from the German Academic Exchange Service (DAAD, 57314023 and 57440918), the Corporation Center of Excellence in Marine Sciences (CEMarin), Fundación para la Promoción de la Investigación y la Tecnología (Banco de la República de Colombia), the Centre de Recerca Matemàtica (CRM) in Barcelona and the ESM-project of the Helmholtz Impulse and Networking Funds. Grants from MCIN/AEI/10.13039/501100011033, and NextGenerationEU/PRTR were also granted to AMGG (FJC2021-047434-I) and ÁG (FEDER, IJC2020-043372-I and PID2021-125979OB-I00). AMGG is grateful with Antoine Jacquey for his advice during early versions of the thermal models and with Maximilian Frick for his guidance on the use of Paraview.

References

Acosta, J., Velandia, F., Osorio, J., Lonergan, L. and Mora, H.: Strike-slip deformation within the Colombian Andes, Geol. Soc. Spec. Publ., 272(January), 303–319, doi:10.1144/GSL.SP.2007.272.01.16, 2007.

ANH: Banco de información petrolera, [online] Available from: https://www.anh.gov.co/Banco de informacion petrolera/EPIS/Paginas/default.aspx (Accessed 21 March 2020), 2020.

Arcila, M., García, J., Montejo, J., Eraso, J., Valcarcel, J., Mora, M., Viganò, D., Pagani, M. and Díaz, F.: Modelo nacional de amenaza sísmica para Colombia., 2020.

Arvidsson, R., Boutet, J. T. and Kulhanek, O.: Foreshocks and aftershocks of the Mw=7.1 , 1992, earthquake in the Atrato region, Colombia, J. Seismol., 6, 1–11, 2002.

Audemard, F. A. M.: Paleoseismicity studies on the Oca-Ancón fault system, northwestern Venezuela, Tectonophysics, 259(1–3), 67–80, doi:10.1016/0040-1951(95)00144-1, 1996.

Avellaneda-Jiménez, D. S., Monsalve, G., León, S. and Gómez-García, A. M.: Insights into Moho depth beneath the northwestern Andean region from gravity data inversion, Geophys. J. Int., 229(3), 1964–1977,

doi:10.1093/gji/ggac041, 2022.

620 Becker, T. W., Lowry, A. R., Faccenna, C., Schmandt, B., Borsa, A. and Yu, C.: Western US intermountain seismicity caused by changes in upper mantle flow, Nature, 524(7566), 458–461, doi:10.1038/nature14867, 2015.

Biegalski, K. F., Bohlin, J., Carter, J. A., Coyne, J., Dompierre, D., Novosel, G. and Rinehart, C.: Formats and protocols for messages – IMS1.0. International Data Center & Science Applications International Corporation. Document SAIC-99/3004., 1999.

625 Bondár, I. and Storchak, D.: Improved location procedures at the International Seismological Centre, Geophys. J. Int., 186(3), 1220–1244, doi:10.1111/j.1365-246X.2011.05107.x, 2011.

Bormann, P.: Are new data suggesting a revision of the current Mw and Me scaling formulas?, J. Seismol., 19(4), 989–1002, doi:10.1007/s10950-015-9507-y, 2015.

Cacace, M. and Jacquey, A. B.: Flexible parallel implicit modelling of coupled thermal-hydraulic-mechanical
630 processes in fractured rocks, Solid Earth, 8(5), 921–941, doi:10.5194/se-8-921-2017, 2017.

Cacace, M. and Scheck-Wenderoth, M.: Why intracontinental basins subside longer: 3-D feedback effects of lithospheric cooling and sedimentation on the flexural strength of the lithosphere, J. Geophys. Res. Solid Earth, 121, 3742–3761, doi:10.1002/2015JB012682, 2016.

Chen, W.-P. and Molnar, P.: Focal depths of intracontinental and intraplate earthquakes and their implications for the
635 thermal and mechanical properties of the lithosphere., J. Geophys. Res., 88(B5), 4183–4214, doi:10.1029/jb088ib05p04183, 1983.

Chen, W. P., Yu, C. Q., Tseng, T. L., Yang, Z., Wang, C. yuen, Ning, J. and Leonard, T.: Moho, seismogenesis, and rheology of the lithosphere, Tectonophysics, 609(January 2021), 491–503, doi:10.1016/j.tecto.2012.12.019, 2013.

Chiarabba, C. and De Gori, P.: The seismogenic thickness in Italy: constraints on potential magnitude and seismic
640 hazard, Terra Nov., 28(6), 402–408, doi:10.1111/ter.12233, 2016.

Dionicio, V. and Sánchez, J. J.: Mapping of B-values, earthquake relocation, and coulomb stress changes during 1992-2007 in the murindó seismic zone, Colombia, J. Seismol., 16(3), 375–387, doi:10.1007/s10950-011-9263-6, 2012.

Efron, B.: Bootstrap methods: another look at the jackknife, Ann. Stat., 7(1), 1–26, 1979.

Ehlers, T. A.: Crustal thermal processes and the interpretation of thermochronometer data, Rev. Mineral.
645 Geochemistry, 58, 315–350, doi:10.2138/rmg.2005.58.12, 2005.

Ferry, N., Parent, L., Garric, G., Barnier, B. and Jourdain, N. C.: Mercator global Eddy permitting ocean reanalysis GLORYS1V1: Description and results, Mercat. Q. Newsl., 34(January), 15–27, 2010.

Gentili, S., Sugan, M., Peruzza, L. and Schorlemmer, D.: Probabilistic completeness assessment of the past 30 years of seismic monitoring in northeastern Italy, Phys. Earth Planet. Inter., 186(1–2), 81–96,
650 doi:10.1016/j.pepi.2011.03.005, 2011.

Gholamrezaie, E., Scheck-Wenderoth, M., Sippel, J. and Strecker, M. R.: Variability of the geothermal gradient across two differently aged magma-rich continental rifted margins of the Atlantic Ocean: The Southwest African and the Norwegian margins, Solid Earth, 9(1), 139–158, doi:10.5194/se-9-139-2018, 2018.

655   Di Giacomo, D. and Storchak, D. A.: A scheme to set preferred magnitudes in the ISC Bulletin, J. Seismol., 20(2), 555–567, doi:10.1007/s10950-015-9543-7, 2016.

Di Giacomo, D., Bondár, I., Storchak, D. A., Engdahl, E. R., Bormann, P. and Harris, J.: ISC-GEM: Global Instrumental Earthquake Catalogue (1900-2009), III. Re-computed MS and mb, proxy MW, final magnitude composition and completeness assessment, Phys. Earth Planet. Inter., 239, 33–47, doi:10.1016/j.pepi.2014.06.005, 2015.

660   Goes, S., Govers, R. and Vacher, P.: Shallow mantle temperatures under Europe from P and S wave tomography, J. Geophys. Res. Earth, 105(B5), 11153–11169, doi:10.1029/1999jb900300, 2000.

Gómez-García, Á. M., González, Á., Cacace, M., Scheck-Wenderoth, M., Monsalve, G.: Hypocentral temperatures, crustal seismogenic thickness and 3D thermal model of the South Caribbean and NW South America. GFZ Data Services. https://doi.org/10.5880/GFZ.4.5.20202.005, 2022

665   Gómez-García, Á. M., Le Breton, E., Scheck-Wenderoth, M., Monsalve, G. and Anikiev, D.: 3D lithospheric structure of the Caribbean and north South American Plates and Rotation Files of Kinematic Reconstructions back to 90 Ma of the Caribbean Large Igneous Plateau. GFZ Data Services. https://doi.org/ 10.5880/GFZ.4.5.2020.003, 2020.

Gómez-García, Á. M., Le Breton, E., Scheck-Wenderoth, M., Monsalve, G. and Anikiev, D.: The preserved plume of the Caribbean Large Igneous Plateau revealed by 3D data-integrative models, Solid Earth, 12(1), 275–298,
670   doi:10.5194/se-12-275-2021, 2021.

González, Á.: The Spanish National Earthquake Catalogue: Evolution, precision and completeness, J. Seismol., 21(3), 435–471, doi:10.1007/s10950-016-9610-8, 2017.

Gutscher, M. A., Klingelhoefer, F., Theunissen, T., Spakman, W., Berthet, T., Wang, T. K. and Lee, C. S.: Thermal modeling of the SW Ryukyu forearc (Taiwan): Implications for the seismogenic zone and the age of the subducting
675   Philippine Sea Plate (Huatung Basin), Tectonophysics, 692, 131–142, doi:10.1016/j.tecto.2016.03.029, 2016.

Hasterok, D., Gard, M. and Webb, J.: On the radiogenic heat production of metamorphic, igneous, and sedimentary rocks, Geosci. Front., 9(6), 1777–1794, doi:10.1016/j.gsf.2017.10.012, 2018.

Hirth, G. and Beeler, N. M.: The role of fluid pressure on frictional behavior at the base of the seismogenic zone, Geology, 43(3), 223–226, doi:10.1130/G36361.1, 2015.

680   Hyndman, R. J. and Fan, Y.: Sample Quantiles in Statistical Packages, Am. Stat., 50(4), 361–365, doi:10.1080/00031305.1996.10473566, 1996.

Jacquey, A. B. & Cacace, M.: GOLEM, a MOOSE-based application v1.0. Zenodo. http://doi.org/10.5281/zenodo.999401, 2017.

Kanamori, H.: The energy release in great earthquakes, , 82(20), 2981–2987, 1977.

685   Kellogg, J. N., Camelio, G. B. F. and Mora-Páez, H.: Cenozoic tectonic evolution of the North Andes with constraints from volcanic ages, seismic reflection, and satellite geodesy, Elsevier Inc., 2019.

Kennan, L. and Pindell, J. L.: Dextral shear, terrane accretion and basin formation in the Northern Andes: best explained by interaction with a Pacific-derived Caribbean Plate?, Geol. Soc. London, Spec. Publ., 328(1), 487–531, doi:10.1144/SP328.20, 2009.

690   Kerr, A. C.: Oceanic Plateaus, in Treatise on Geochemistry: Second Edition, vol. 4, pp. 631–667, Elsevier Ltd., Oxford., 2014.

Klitzke, P., Luzi-Helbing, M., Schicks, J. M., Cacace, M., Jacquey, A. B., Sippel, J., Scheck-Wenderoth, M. and Faleide, J. I.: Gas hydrate stability zone of the Barents Sea and Kara Sea region, Energy Procedia, 97, 302–309, doi:10.1016/j.egypro.2016.10.005, 2016.

695   Laske, G., Masters, G., Ma, Z., & Pasyanos, M. E.: CRUST1.0: An Updated Global Model of Earth's Crust. Geophys. Res. Abstracts, 15, Abstract EGU2013--2658. Retrieved from http://igppweb.ucsd.edu/~gabi/rem.html, 2013.

León, S., Cardona, A., Parra, M., Sobel, E., et al: Transition From Collisional to Subduction-Related Regimes: An Example From Neogene Panama-Nazca-South America Interactions. Tectonics, 37(1), 119-139, 2018.

Li, Y. and Toksoz, N.: Study of the source process of the 1992 Colombia Ms=7.3 earthquake with the empirical
700   Green's function method, Geophys. Res. Lett., 20(11), 1087–1090, 1993.

Lucazeau, F.: Analysis and mapping of an updated terrestrial heat flow data set, Geochemistry, Geophys. Geosystems, 4001–4024, doi:10.1029/2019gc008389, 2019.

Marcaillou, B., Charvis, P. and Collot, J. Y.: Structure of the Malpelo Ridge (Colombia) from seismic and gravity modelling, Mar. Geophys. Res., 27(4), 289–300, doi:10.1007/s11001-006-9009-y, 2006.

705   Marone, C. and Saffer, D. M.: The Mechanics of Frictional Healing and Slip Instability During the Seismic Cycle, Elsevier B.V., 2015.

Marone, C. and Scholz, C. H.: The depth of seismic faulting and the upper transition from stable to unstable slip regimes, Geophys. Res. Lett., 15(6), 621–624, doi:10.1029/GL015i006p00621, 1988.

Martínez, J. M., Parra, E., Paris, G., Forero, C., Bustamante, M., Cardona, O. D. & Jaramillo, J. D.: Los sismos del
710   Atrato Medio 17 y 18 de Octubre de 1992 Noroccidente de Colombia. Revista Ingeominas, 4, 35–76, 1994.

McKenzie, D., Jackson, J. and Priestley, K.: Thermal structure of oceanic and continental lithosphere, Earth Planet. Sci. Lett., 233(3–4), 337–349, doi:10.1016/j.epsl.2005.02.005, 2005.

Meeßen, C.: VelocityConversion, , doi:http://doi.org/10.5880/GFZ.6.1.2017.001, 2017.

Molchan, G. M.: Strategies in strong earthquake prediction, Phys. Earth Planet. Inter., 61(1–2), 84–98,
715   doi:10.1016/0031-9201(90)90097-H, 1990.

Molchan, G. M.: Structure of optimal strategies in earthquake prediction, Tectonophysics, 193(4), 267–276, doi:10.1016/0040-1951(91)90336-Q, 1991.

Molchan, G. M. and Kagan, Y. Y.: Earthquake prediction and its optimization, J. Geophys. Res., 97(B4), 4823–4838, doi:10.1029/91JB03095, 1992.

720   Montes, C., Rodriguez-Corcho, A. F., Bayona, G., Hoyos, N., Zapata, S. and Cardona, A.: Continental margin response to multiple arc-continent collisions: The northern Andes-Caribbean margin, Earth-Science Rev., 198(July), 102903, doi:10.1016/j.earscirev.2019.102903, 2019.

Mora-Bohórquez, J. A., Oncken, O., Le Breton, E., Mejia-Ibañez, M., Veloza, G., Mora, A., Vélez, V. and De Freitas,

725   M.: Formation and Evolution of the Lower Magdalena Valley Basin and San Jacinto Fold Belt of Northwestern Colombia: Insights from Upper Cretaceous to Recent Tectono-Stratigraphy, in The Geology of Colombia, Volume 3 Paleogene – Neogene. Servicio Geológico Colombiano, Publicaciones Geológicas Especiales., vol. 3, edited by J. Gómez and D. Mateus–Zabala, pp. 21–66., 2020.

Mosquera-Machado, S., Lalinde-Pulido, C., Salcedo-Hurtado, E. and Michetti, A. M.: Ground effects of the 18 October 1992, Murindo earthquake (NW Colombia), using the Environmental Seismic Intensity Scale (ESI 2007) for 730   the assessment of intensity, Geol. Soc. Spec. Publ., 316, 123–144, doi:10.1144/SP316.7, 2009.

Muñoz Sabater, J.: ERA5-Land monthly averaged data from 1981 to present. Copernicus Climate Change Service (C3S) Climate Data Store (CDS). (Accessed on 15-09-2019), 10.24381/cds.68d2bb3, 2019.

Neill, I., Kerr, A. C., Hastie, A. R., Stanek, K.-P. and Millar, I. L.: Origin of the Aves Ridge and Dutch-Venezuelan Antilles: interaction of the Cretaceous "Great Arc" and Caribbean-Colombian Oceanic Plateau?, J. Geol. Soc. 735   London., 168(2), 333–348, doi:10.1144/0016-76492010-067, 2011.

Noriega-Londoño, S., Restrepo-Moreno, S. A., Vinasco, C., Bermúdez, M. A. and Min, K.: Thermochronologic and geomorphometric constraints on the Cenozoic landscape evolution of the Northern Andes: Northwestern Central Cordillera, Colombia, Geomorphology, 351, doi:10.1016/j.geomorph.2019.106890, 2020.

Oleskevich, D., Hyndman, R. and Wang, K.: The updip and downdip limits to great subduction earthquakes: Thermal 740   and structural models of Cascadia, south Alaska, SW Japan, and Chile, J. Geophys. Res., 104(B7), 14965–14991, 1999.

Pagani, M., García-Pelaez, J., Gee, R., Johnson, K., Poogi, R., Styron, G., Weatherill, M., Simionato, D., Viganò, D., Danciu, L. and Monelli, D.: Global Earthquake Model (GEM) Seismic Hazard Map (version 2018.1 - December 2018), , doi:10.13117/GEM-GLOBAL-SEISMIC-HAZARD-MAP-2018.1, 2018.

745   Paris, G., Machette, M. N., Dart, R. L. and Haller, K. M.: Map and database of Quaternary faults and folds in Colombia and its offshore regions., 2000.

Pavlis, N. K., Holmes, S. A., Kenyon, S. C. and Factor, J. K.: The development and evaluation of the Earth Gravitational Model 2008 (EGM2008), J. Geophys. Res. Solid Earth, 117(4), 1–38, doi:10.1029/2011JB008916, 2012.

750   Pousse-Beltran, L., Vassallo, R., Audemard, F., Jouanne, F., Oropeza, J., Garambois, S. and Aray, J.: Earthquake geology of the last millennium along the Boconó Fault, Venezuela, Tectonophysics, 747–748(January), 40–53, doi:10.1016/j.tecto.2018.09.010, 2018.

Poveda, E., Monsalve, G. and Vargas, C.: Receiver functions and crustal structure of the northwestern Andean region, Colombia, J. Geophys. Res. Solid Earth, (120), 2408–2425, doi:10.1002/2014JB011304., 2015.

755   Poveda, E., Julià, J., Schimmel, M. and Perez-Garcia, N.: Upper and Middle Crustal Velocity Structure of the Colombian Andes From Ambient Noise Tomography: Investigating Subduction-Related Magmatism in the Overriding Plate, J. Geophys. Res. Solid Earth, 123(2), 1459–1485, doi:10.1002/2017JB014688, 2018.

Reguzzoni, M. and Sampietro, D.: GEMMA: An Earth crustal model based on GOCE satellite data, Int. J. Appl. Earth Obs. Geoinf., 35(PA), 31–43, doi:10.1016/j.jag.2014.04.002, 2015.

760   Restrepo, J. J. and Toussaint, J. F.: Terranes and continental accretion in the Colombian Andes, Episodes, 11(3), 189–

193, doi:10.18814/epiiugs/1988/v11i3/006, 1988.

Rodriguez Piceda, C., Scheck-Wenderoth, M., Cacace, M., Bott, J. and Strecker, M. R.: Long-Term Lithospheric Strength and Upper-Plate Seismicity in the Southern Central Andes, 29°–39°S, Geochemistry Geophys. Geosystems, 23(e2021GC010171), doi:10.1029/2021GC010171, 2022.

765 Salazar, W., Brown, L., Hernández, W. and Guerra, J.: An Earthquake Catalogue for El Salvador and Neighboring Central American Countries (1528-2009) and Its Implication in the Seismic Hazard Assessment, J. Civ. Eng. Archit., 7(8), 1018–1045, doi:10.17265/1934-7359/2013.08.011, 2013.

Schaeffer, A. J. and Lebedev, S.: Global shear speed structure of the upper mantle and transition zone, Geophys. J. Int., 194(1), 417–449, doi:10.1093/gji/ggt095, 2013.

770 Scheck-Wenderoth, M. and Maystrenko, Y. P.: Deep control on shallow heat in sedimentary basins, Energy Procedia, 40, 266–275, doi:10.1016/j.egypro.2013.08.031, 2013.

Scholz, C. H.: The Mechanics of Earthquakes and Faulting, 3rd Editio., Cambridge University Press., 2019.

Sibson, R.: Fault zone models, heat flow, and the depth distribution of earthquakes in the continental crust of the United States, Bull. Seism. Soc. Am., 72(1), 151–163, 1982.

775 Silva, V., Amo-Oduro, D., Calderon, A., Dabbeek, J., Despotaki, V., Martins, L., Rao, A., Simionato, M., Viganò, D., Yepes-Estrada, C., Acevedo, A., Crowley, H., Horspool, N., Jaiswal, K., Journeay, M. and Pittore, M.: Global Earthquake Model (GEM) Seismic Risk Map (version 2018.1), , doi:10.13117/GEM-GLOBAL-SEISMIC-RISK-MAP- 2018, 2018.

Storchak, D. A., Harris, J., Brown, L., Lieser, K., Shumba, B. and Di Giacomo, D.: Rebuild of the Bulletin of the
780 International Seismological Centre (ISC)—part 2: 1980–2010, Geosci. Lett., 7(1), doi:10.1186/s40562-020-00164-6, 2020.

Styron, R., García-Pelaez, J. and Pagani, M.: CCAF-DB: The Caribbean and Central American active fault database, Nat. Hazards Earth Syst. Sci., 20(3), 831–857, doi:10.5194/nhess-20-831-2020, 2020.

Sun, M., Bezada, M. J., Cornthwaite, J., Prieto, G. A., Niu, F. and Levander, A.: Overlapping slabs: Untangling
785 subduction in NW South America through finite-frequency teleseismic tomography, Earth Planet. Sci. Lett., 577, 117253, doi:10.1016/j.epsl.2021.117253, 2022.

Tse, S. T. and Rice, J. R.: Crustal earthquake instability in relation to the depth variation of frictional slip properties, J. Geophys. Res., 91(B9), 9452, doi:10.1029/jb091ib09p09452, 1986.

Turcotte, D. and Schubert, G.: Geodynamics. Cambridge. https://doi.org/10.1017/CBO9781107415324.004, 2002.

790 Veloza, G., Styron, R. and Taylor, M.: Open-source archive of active faults for northwest South America, GSA Today, 22(10), 4–10, doi:10.1130/GSAT-G156A.1, 2012.

Vilà, M., Fernández, M. and Jiménez-Munt, I.: Radiogenic heat production variability of some common lithological groups and its significance to lithospheric thermal modeling, Tectonophysics, 490(3–4), 152–164, doi:10.1016/j.tecto.2010.05.003, 2010.

795 Weatherall, P., Marks, K. M., Jakobsson, M., Schmitt, T., Tani, S., Arndt, J. E., Rovere, M., Chayes, D., Ferrini, V.

and Wigley, R.: A new digital bathymetric model of the world's oceans, Earth Sp. Sci., 2, 331–345, doi:10.1002/2015EA000107, 2015.

Wessel, P. & Smith, W. H. F.: Free software helps map and display data, EOS Trans. AGU, 72, 441, 1991.

800 Wiemer, S. and Wyss, M.: Mapping the frequency-magnitude distribution in asperities: An improved technique to calculate recurrence times?, J. Geophys. Res. Solid Earth, 102(B7), 15115–15128, doi:10.1029/97jb00726, 1997.

Wiemer, S. and Wyss, M.: Minimum magnitude of completeness in earthquake catalogs: Examples from Alaska, the Western United States, and Japan, Bull. Seismol. Soc. Am., 90(4), 859–869, doi:10.1785/0119990114, 2000.

Woessner, J. and Wiemer, S.: Assessing the quality of earthquake catalogues: Estimating the magnitude of completeness and its uncertainty, Bull. Seismol. Soc. Am., 95(2), 684–698, doi:10.1785/0120040007, 2005.

805 Wu, W. N., Yen, Y. T., Hsu, Y. J., Wu, Y. M., Lin, J. Y. and Hsu, S. K.: Spatial variation of seismogenic depths of crustal earthquakes in the Taiwan region: Implications for seismic hazard assessment, Tectonophysics, 708, 81–95, doi:10.1016/j.tecto.2017.04.028, 2017.

Zechar, J. D. and Jordan, T. H.: Testing alarm-based earthquake predictions, Geophys. J. Int., 172(2), 715–724, doi:10.1111/j.1365-246X.2007.03676.x, 2008.

810 Zielke, O., Schorlemmer, D., Jónsson, S. and Mai, P. M.: Magnitude-dependent transient increase of seismogenic depth, Seismol. Res. Lett., 91(4), 2182–2191, doi:10.1785/0220190392, 2020.

Zuza, A. V. and Cao, W.: Seismogenic thickness of California: Implications for thermal structure and seismic hazard, Tectonophysics, 782–783(April), 228426, doi:10.1016/j.tecto.2020.228426, 2020.